Ore Geology Reviews 152 (2023) 105256

Contents lists available at ScienceDirect

Ore Geology Reviews

journal homepage: www.elsevier.com/locate/oregeorev

The distribution of trace elements in sulfides and magnetite from the Jaguar hydrothermal nickel deposit: Exploring the link with IOA and IOCG deposits within the Carajás Mineral Province, Brazil

Eduardo T. Mansur [a,b,*], Sarah A.S. Dare [b], Cesar F. Ferreira Filho [c], Ana Carolina Rodrigues Miranda [d], Lena Virginia Soares Monteiro [e]

[a] Geological Survey of Norway, PO Box 6315, Torgarden, Trondheim 7491, Norway
[b] Département de Sciences Appliquées, Université du Québec à Chicoutimi, QC G7H 2B1, Canada
[c] Instituto de Geociências, Universidade de Brasília, Brasília, DF 70910-900, Brazil
[d] Département de géologie et de génie géologique, Université Laval, QC G1V 0A6, Canada
[e] Institute of Geosciences, University of São Paulo R. do Lago, 562 05508-080 São Paulo, SP, Brazil

ARTICLE INFO

Keywords:
Hydrothemal nickel
IOA-IOCG deposits
Carajás Mineral Province
Trace elements
Magnetite
Base metal sulfides

ABSTRACT

The Jaguar nickel deposit represents an important and unconventional discovery of hydrothermal Ni resources (58.9 Mt @ 0.95% Ni) associated with magnetite and apatite within the Carajás Mineral Province, Northern Brazil. The Jaguar deposit shares several similarities with iron oxide copper–gold (IOCG) deposits of the Carajás Mineral Province, especially regarding the structural control, and the hydrothermal alteration. Although IOCG and Kiruna-type iron oxide-apatite (IOA) deposits are closely associated in several geological provinces, this association has not yet been fully constrained in the Carajás Mineral Province. The Jaguar deposit occurs near mafic–ultramafic intrusions, along a regional fault zone, and is hosted either by granitic (northern portion) or felsic subvolcanic (southern portion) rocks. It is characterized by sub-vertical zones hosting a biotite-chlorite (Bt-Chl) hydrothermal alteration with ductile structures and disseminated sulfides (pyrite and millerite) and magnetite. These zones are overprinted by sulfide-magnetite-apatite-bearing breccias, which represent the main mineralization bodies. The sulfide assemblage in the mineralized zones is dominated by pyrite, pentlandite and millerite, with minor sphalerite and chalcopyrite.

We have investigated the concentration of trace elements in the magnetite and sulfides from the host rocks, different alteration facies and the mineralization at the Jaguar deposit by LA-ICP-MS. Magnetite composition ranges from higher Al, Mn, Ti and V contents, for at least part of those in host rocks (granitic and felsic subvolcanic) and Bt-Chl alteration, into lower contents in the magnetite-apatite alteration, associated with the main Ni mineralization. Magnetite with higher Ti and V contents in host rocks is associated with discrete hydrothermal alteration pockets, have high Ni/Cr ratios and plot in high temperature hydrothermal fields in multi-element diagrams. Therefore, we support that these features are compatible with a hydrothermal origin. Anomalously high-Ni contents in magnetite point that the Neoarchean mafic–ultramafic layered intrusions of the Carajás Province represent potential Ni sources for hydrothermal remobilization. Anomalously high V contents in magnetite suggest lower fO_2 conditions upon the formation of the deposit. The concentration of trace elements in magnetite associated with the Jaguar deposit is similar to those from other IOCG deposits from the Carajás Province (but with higher V and Ni contents), especially the Sossego mine in the Southern Copper Belt, indicating that it could represent a Ni-rich member of the regional-scale IOCG mineral system at Carajás. Pyrite and chalcopyrite have a composition similar to those from magmatic deposits, when using previously proposed discriminant diagrams, but this is also the case for other IOA and IOCG deposits. However, low PGE contents (Ru, Rh, Ir and Os) in pyrite from the Jaguar deposit support a hydrothermal origin. Our results highlight that the classifications provided by available discriminant diagrams are not unequivocal. We suggest that multi-element diagrams represent a complementary approach to binary plots and provide a more comprehensive classification for the use of indicator minerals.

* Corresponding author.
E-mail address: eduardo.mansur@ngu.no (E.T. Mansur).

https://doi.org/10.1016/j.oregeorev.2022.105256
Received 10 June 2022; Received in revised form 1 November 2022; Accepted 10 December 2022
Available online 12 December 2022

1. Introduction

Iron oxide copper–gold (IOCG) and iron oxide-apatite (IOA - Kiruna-type) deposits are spatially and temporally associated in several mineral districts (Simon et al., 2018 and references therein). Some studies suggest that these define a continuum with IOA deposits representing deeper portions at a higher temperature, whereas IOCG deposits represent shallower and lower temperature portions of the same regional-scale hydrothermal system (Knipping et al., 2015; Corriveau et al., 2016; Barra et al., 2017; Palma et al., 2019; Rodriguez-Mustafa et al., 2022). The Carajás Mineral Province, Northern Brazil, is known for the presence of several IOCG deposits with magnetite-(apatite)-rich zones that represent the locus of later copper–gold mineralization (Grainger et al., 2008; Monteiro et al., 2008a; Xavier et al., 2010, 2012,2017; Moreto et al., 2015; Schutesky and de Oliveira, 2020). However, no typical IOA deposit was found in the province until recently. Therefore, there is still a lack of understanding whether the connection between IOA and IOCG deposits also occurs in the Carajás Province. Recent contributions suggest that Ni-rich hydrothermal deposits (e.g. GT-34 deposit) may represent deeper members of the IOCG system of the Carajás Mineral Province (Garcia et al., 2020; Schutesky and de Oliveira, 2020; Pestilho et al., 2020; Veloso et al., 2020), but whether these are potentially IOA equivalents is not yet fully constrained.

There is much discussion about the mechanisms that lead to the formation of IOA and IOCG deposits, and their eventual relationship. Some authors support an initially magmatic origin that further evolves into a magmatic-hydrothermal system (e.g. Knipping et al., 2015; Simon et al., 2018; Palma et al., 2019; Xie et al., 2019; Rodriguez-Mustafa et al., 2022), others argue for a dominantly hydrothermal model (Sillitoe and Burrows, 2002; Mumin et al., 2007; Dare et al., 2015; Corriveau et al., 2016), whereas experiments also suggest the participation of an immiscible Fe-P melt (Lester et al., 2013a; Tornos et al., 2017; Velasco et al., 2016; Hou et al., 2018; Bain et al., 2020). Therefore, precisely identifying different members of regional-scale IOA or IOCG systems, and obtaining some constraint on their evolution, is a key step for refining the genetic model of these controversial deposits. Moreover, assessing the main characteristics of different members of the regional scale IOCG system from the Carajás Province may support future exploration and discovery of new mineral deposits in the region.

The Jaguar nickel deposit represents an important discovery of hydrothermal Ni resources (58.9 Mt @ 0.95 % Ni) associated with base metal sulfides, magnetite and apatite within the Carajás Mineral Province (Oliveira, 2017; Ferreira Filho et al., 2021). The Jaguar deposit shares several similarities with IOCG deposits within the Carajás Mineral Province, especially regarding the structural control by shear zones or faults, and high-T Fe-Ca hydrothermal alteration (Corriveau et al., 2016). These similarities raise the possibility that the Jaguar deposit may represent a Ni-rich IOA member of the regional IOCG system found within the province. For instance, based on similarities in structural control, alteration zones and whole-rock geochemistry, Ferreira Filho et al. (2021) suggested that the deposit is part of the IOCG clan in the Carajás Province, but this hypothesis has yet to be tested more comprehensively. Therefore, the Jaguar deposit offers the opportunity to explore possible variations within a regional-scale hydrothermal system, and to evaluate further the mechanisms by which these deposits are connected.

This contribution investigates the concentration of trace elements in base metal sulfides (BMS) and Fe-oxides (magnetite) from the different rock types found in the Jaguar deposit and its surroundings. Trace element contents in both BMS and magnetite have been shown to record several ore-forming processes, and thus represent a powerful tool for studying different mineral systems. Our results are compared with those from other IOA and IOCG deposits worldwide and with the available results for the IOCG deposits from the Carajás Mineral Province. The distribution of trace elements in BMS and magnetite provides constraints on the mechanisms that led to the formation of the Jaguar Ni deposit and supports a hydrothermal origin for the Ni ores. Moreover, the results also demonstrate the risks of using binary discriminant diagrams for the classification of different deposit types in a straightforward manner (e.g. Dupuis and Beaudoin, 2011; Dare et al., 2014; Duran et al., 2015; Deditius et al., 2018) as these diagrams may provide misleading interpretations if used in an uncensored fashion.

2. Regional setting

The Carajás Province is located in the southeastern margin of the Amazon Craton in Brazil (Fig. 1a) and is one of the best-preserved Archean cratonic areas in the world. It is limited to the east and south by the Neoproterozoic Araguaia Fold Belt and, to the west, by Proterozoic sequences of the Uatumã Supergroup (DOCEGEO, 1988; Araújo and Maia, 1991; Silva et al., 2021). To the north, it is limited by the Bacajá Domain, which includes reworked Archean terrains and juvenile Paleoproterozoic units (Vasquez et al., 2008a). The Carajás Province was divided into two Archean domains: the southern Rio Maria and the northern Carajás domains (Fig. 1b; Vasquez et al., 2008a). A poorly defined zone characterized by regional EW faults, designated as the Transition Subdomain (Feio et al., 2013), separates these two domains.

The Rio Maria Domain is a granite–greenstone terrain comprising greenstone sequences and *meta*-sedimentary rocks of the 2.97 to 2.90 Ga Andorinhas Supergroup (DOCEGEO, 1988; Macambira and Lancelot, 1996; Souza et al., 2001). The Rio Maria Domain hosts orogenic gold deposits (e.g., Grainger et al., 2008). The Carajás Domain basement units consist of gneisses and migmatites of the Xingu Complex and mafic to felsic *ortho*-granulites of the Chicrim-Cateté Orthogranulite (DOCEGEO, 1988; Machado et al., 1991; Pidgeon et al., 2000). Overlying the basement units is the Neoarchean Carajás Basin. It comprises the ca. 2.73 to 2.76 Ga metavolcanic-sedimentary units of the Itacaiúnas Supergroup (Wirth et al., 1986; DOCEGEO, 1988; Machado et al., 1991). The Grão Pará Group, the dominant volcanic-sedimentary unit in the Carajás Basin, contains the giant iron deposits of the Carajás Mineral Province (DOCEGEO, 1988; Vasquez et al., 2008a). The Itacaiúnas Supergroup is overlain by an extensive succession of low-grade *meta*-sedimentary units known as the Águas Claras Formation (Nogueira, 1985; Araújo and Nogueira, 2019) or the Rio Fresco Group (DOCEGEO, 1988).

The Carajás Basin was crosscut by granitic rocks with distinct ages and compositions (e.g., Feio et al., 2013). They are correlated with three episodes of magmatism: (1) Neoarchean intrusions (ca. 2.75–2.70 Ga) are widespread through the Carajás Domain and include *syn*-orogenic alkaline granites; (2) Younger Neoarchean intrusions (ca. 2.5 Ga) that are restricted to the north part of the Carajás Domain and include peralkaline to *meta*-aluminous granites, coeval with the Carajás and Cinzento transcurrent fault systems: (3) Paleoproterozoic intrusions (ca. 1.88 Ga) are widespread in the Carajás Mineral Province and Rio Maria Domain and include A-type alkaline granites. The tectonic setting of the Carajás Basin is still a matter of debate, in which the mafic rocks of the Itacaiúnas Supergroup have been interpreted as part of a continental extensional basin (e.g., Gibbs et al., 1986; DOCEGEO, 1988; Araújo and Maia, 1991; Trunfull et al., 2020), related to mantle plume activity (Tallarico et al., 2005) and compressional orogenic settings (e. g., fore- or back-arc basin; Silva et al., 2005; Zucchetti, 2007).

2.1. The mafic–ultramafic layered intrusions in the Carajás mineral Province

The Carajás Mineral Province contains the largest concentration of mafic–ultramafic layered intrusions in the Amazonian Craton. These intrusions are best known for hosting world-class Ni-laterite deposits (e. g., Jacaré-Jacarezinho, Vermelho and Puma-Onça; Ferreira Filho et al., 2007; Rosa, 2014; Siepierski and Ferreira Filho, 2020), and PGE deposits and occurrences (e.g., Luanga and Lago Grande Complexes; Ferreira

Filho et al., 2007; Teixeira et al., 2015; Mansur and Ferreira Filho, 2016; Mansur and Ferreira Filho, 2017; Mansur et al., 2020a). Neoarchean (ca. 2.76 Ga) zircon U-Pb ages of the layered intrusions overlap with ages of bimodal volcanism in the province, supporting the interpretation that they formed from a major coeval event (Machado et al., 1991; Ferreira Filho et al., 2007).

Layered intrusions hosting word-class nickel laterite deposits are abundant in the south portion of the Carajás Province and include the Serra da Onça and Serra do Puma complexes (Ferreira Filho et al., 2007; Rosa, 2014), located close to the Jaguar deposit (Fig. 1b). Both layered intrusions are emplaced into banded gneiss-migmatite of the Xingu Complex and/or slightly foliated granitic intrusions. The Serra da Onça Complex is a 24 km long and up to 3.5 km wide EW trending intrusion, with magmatic layering dip of 40-45° to the south. The stratigraphy of the Serra da Onça Complex consists of a Lower Border Group at the base, an Ultramafic Zone (up to 1.1 km thick), and an upper Mafic Zone (up to 1.5 km thick). The Serra do Puma Complex is a 25 km long and up to 3 km wide SW-NE trending layered intrusion, with magmatic layering consistent dip of 30-40° to the southeast. Similar to the Serra da Onça intrusion, the stratigraphy consists of a discontinuous Lower Border Group at the base, an Ultramafic Zone (up to ~ 1.0 km thick), and an upper Layered Zone (up to ~ 1.1 km thick).

The composition of the parental magmas of the layered intrusions from the Carajás Mineral Province cannot be constrained by common approaches used in well-exposed and unaltered intrusions (e.g., chilled margin, bulk composition, extrusive equivalents, related dykes, and melt inclusions) (Mansur and Ferreira Filho, 2016). The most-magnesium olivine compositions of several layered intrusions in the province indicate primitive parental magmas, as illustrated by forsterite contents from Serra da Onça (up to 92.4 mol%) and Serra do Puma (up to 87.7 mol%) complexes. Secondary assemblages commonly replace primary igneous minerals of the layered intrusions in the Carajás Mineral Province. The post-magmatic alteration is heterogeneous and characterized by an extensive hydration that locally preserves primary

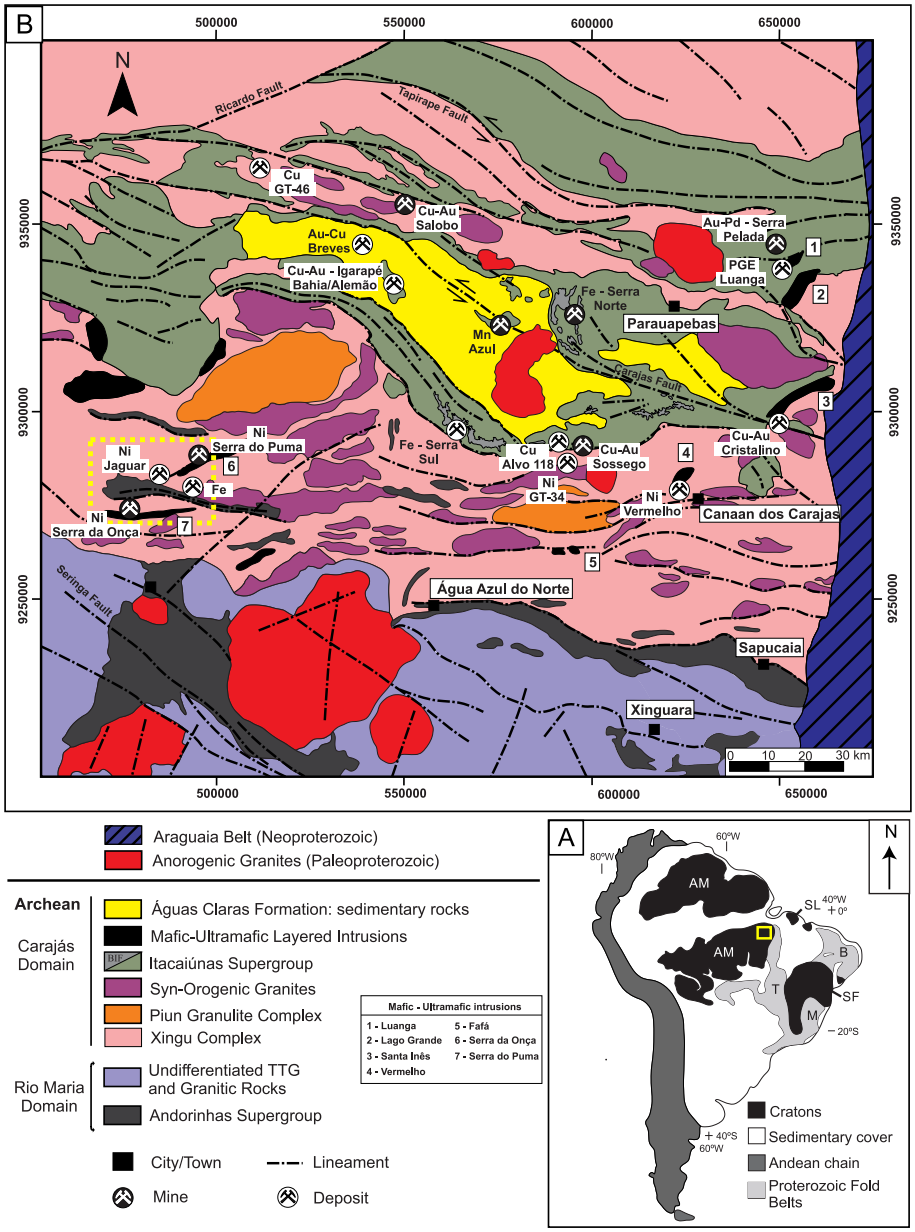

Fig. 1. Regional geology of the Carajás Mineral Province, Brazil. a) Location of the Carajás Mineral Province. AM - Amazonian Craton; B - Borborema Province; M - Mantiqueira Province; SF - São Francisco Craton; T - Tocantins Province. b) Geology and mineral deposits of the Carajás Mineral Province (partially modified from Vasquez et al., 2008b). The dashed rectangle indicates the position of the Jaguar deposit.

textures, bulk rock compositions and the compositional domains of igneous minerals. Metamorphic assemblages indicate temperatures up to the amphibolite facies of metamorphism, but commonly greenschist facies.

2.2. The IOCG deposits in the Carajás mineral Province

The IOCG deposits of the Carajás Mineral Province are located along or close to regional shear zones, hosted within units of the Itacaiúnas Supergroup or basement rocks of the Xingu Complex (e.g., Grainger et al., 2008; Xavier et al., 2012, 2017; Schutesky and de Oliveira, 2020). They are mainly located in two sectors of the Carajás Mineral Province: the northern copper belt and the southern copper belt. The northern copper belt occurs along the W-NW- striking Cinzento shear zone (Fig. 1B) and hosts the Salobo (Cu-Au), Igarapé Bahia-Alemão (Cu-Au) and Alvo GT-46 (Cu) deposits, as well as several other deposits (e.g., Grota Funda, Paulo Afonso, Gameleira). The southern copper belt occurs along a W-NW- striking, 60 km long shear zone and includes the Sossego (Cu-Au), Cristalino (Cu-Au), Alvo 118 (Cu) deposits (Fig. 1B), as well as several satellite deposits (e.g., Visconde, Castanha, Bacaba, Jatobá and Bacuri).

Although spatially separated, the IOCG deposits from the northern and southern belts share several geological and geochemical characteristics. The host rocks are variable for different IOCG deposits in the Carajás Mineral Province, including rocks from metavolcanic-sedimentary units of the Itacaiúnas Supergroup, as well as felsic and mafic intrusive rocks (e.g., Xavier et al., 2012). Typical hydrothermal alteration assemblages characterize different IOCG deposits in the Carajás Mineral Province (Craveiro et al., 2019; de Melo et al., 2021). They commonly display an early high-temperature (greater than500 °C) sodic-calcic alteration controlled by ductile structures and mylonitic fabrics. This sodic-calcic alteration is characterized by variable amounts of albite and actinolite (e.g., Sequeirinho ore body in the Sossego deposit; Monteiro et al., 2008a; Monteiro et al., 2008b; Xavier et al., 2012) or scapolite. Similar high-temperature alteration assemblages in the Salobo deposit (de Melo et al., 2017; Campo-Rodríguez et al., 2021; Huang and Beaudoin, 2021) were used to suggest emplacement at relatively deep crustal levels (e.g., Réquia et al., 2003). Ferric-calcic (magnetite-apatite-actinolite) or ferric-potassic (biotite-magnetite) alteration zones represent the locus of main copper precipitation controlled by ductile structures. Following this ductile early stage, some deposits display a potassic (K-feldspar and biotite) alteration frequently overprinted by lower temperature (<300 °C) chlorite, carbonate-epidote, or sericite-hematite alteration and associated later Cu-Au mineralization. Both the potassic and lower temperature alteration are controlled by brittle structures (e.g., Sossego ore body at Sossego; Monteiro et al., 2008a; 2008b; and Alvo 118; Torresi et al., 2012). Potassic, chlorite, silica, and carbonate alteration are important in deposits that underwent late (Paleoproterozoic) alteration under brittle-ductile conditions at shallower crustal levels (e.g., Igarapé Bahia, Cristalino, Sossego, and Alvo 118; Xavier et al., 2012; de Melo et al., 2019).

The geochemical signature of the IOCG deposits of the Carajás Mineral Province is defined by high contents of Fe-Cu-Au-LREE-P in most deposits, as well as anomalously high contents of U-Ni-Co-Pd-Y-sn-Bi-Be-Pb-Ag-Te (Xavier et al., 2010). The geometry of IOCG deposits is generally dependent on the crustal depth: lens-shaped and massive replacement bodies parallel to the mylonitic foliation occur at deeper crustal levels (e.g., Sabobo; Souza and Vieira, 2000), whereas brecciated bodies and vein stockworks are dominant in shallower systems (Xavier et al., 2012). Ore mineral assemblages overprint early magnetite-rich alteration in the IOCG deposits in Carajás (e.g., Xavier et al., 2012; Craveiro et al., 2019). These reveal variable sulfidation states of the source fluids: chalcopyrite-chalcocite-bornite-magnetite at Salobo (e.g., Réquia et al., 2003); chalcopyrite ± chalcocite-digenite-covellite-magnetite at Igarapé Bahia (e.g., Tazava et al., 1999; Dreher et al., 2008); chalcopyrite-pyrite-magnetite at Sossego (e.g., Xavier et al., 2012) and Cristalino (Huhn et al., 1999); and chalcopyrite-bornite-hematite at Alvo 118 (Torresi et al., 2012).

Several recent studies have also indicated the occurrence of Ni mineralization in hydrothermal systems spatially associated with the IOCG deposits in the region, notably in the southern belt. For instance, the GT-34 prospect (Siepierski, 2008; Garcia et al., 2020), the Jaguar deposit (Oliveira, 2017; Ferreira Filho et al., 2021), as well as Ni mineralization associated with the Castanha (Pestilho et al., 2020) and Jatobá (Veloso et al., 2020) IOCG deposits. These contributions indicate that hydrothermal Ni mineralization and IOCG deposits share common features in the Carajás Mineral Province, including their association with metavolcanic-sedimentary sequences, intense Fe-Ca hydrothermal alteration, location along major fault systems and ore breccias. Thus, they may be part of the same regional scale hydrothermal system.

Although numerous contributions have been dedicated to the study of the IOCG systems in the Carajás Mineral Province, the spatial and temporal relationship between intrusions and IOCG ore bodies is not yet fully constrained. Early studies proposed that the genesis of the IOCG mineralization in Carajás was related to two major granitic events (e.g., Tallarico et al., 2005; Grainger et al., 2008): (1) a major Archean event at ca. 2.57 Ga (Salobo, Igarapé Bahia-Alemão, Cristalino and Sossego deposits), related to the Old Salobo and Itacaiúnas granites and (2) a major Paleoproterozoic event at ca. 1.88 Ga (Alvo 118 deposit), related to the Central de Carajás, Young Salobo, Cigano, Pojuca, and Breves granites. However, recent studies suggest that the Southern Copper Belt endured episodic and multiple hydrothermal events over an extended period, from the Neoarchean to the Paleoproterozoic (Moreto et al., 2015). Moreto et al. (2015) showed that several deposits of the southern belt (e.g., Bacaba, Bacuri, and possibly the Castanha, Jatobá, Cristalino, and Visconde; Pestilho et al., 2020; Veloso et al., 2020) record a Neoarchean hydrothermal evolution and share a common metallogenic history with the ca. 2.72–2.68 Ga Sequeirinho-Baiano-Pista ore bodies of the Sossego deposit. Robust geochronological data in the Northern Copper Belt (e.g., Salobo and Igarapé Bahia-Alemão deposits) also indicate an important metallogenetic event at 2.57 Ga (Réquia et al., 2003; Tallarico et al., 2005), which correlates to reported late Archean magmatism in Carajás (Old Salobo and Itacaiúnas granites) or with the Cinzento shear zone reactivation (de Melo et al., 2018).

3. Hydrothermal Ni mineralization and the Jaguar Ni deposit

The Jaguar deposit (Ferreira Filho et al., 2021) is located in the southwestern portion of the Carajás Domain, close to the contact with the Rio Maria Domain (Fig. 1b). It occurs along the intersection of the WNW-ESE-trending Canaã fault system and the NE-SW McCandless fault. In this area, the Xingu Complex consists of banded felsic gneisses and migmatites intruded by large granitic intrusions and mafic–ultramafic layered intrusions, such as the Serra do Puma and Serra da Onça Complexes (Macambira and Ferreira Filho, 2002; Ferreira Filho et al., 2007; Rosa, 2014). Moreover, the banded iron formations (BIF) of the Serra Arqueada, associated with a bimodal volcanic-sedimentary sequence, define an up to 300 m high arc-shaped ridge near the deposit (Fig. 1). Granitic intrusions, mafic–ultramafic layered intrusions, volcanic-sedimentary rocks and gneiss-migmatite from the Xingu Complex are variably affected by potassic hydrothermal alteration near the Jaguar deposit. For a detailed description of the local geology of the Jaguar deposit and surrounding rocks the readers are directed to Ferreira Filho et al. (2021), whereas a few characteristics are summarized here for the purpose of our study.

The Jaguar deposit consists of a 3 km long corridor of WNW discontinuous lens-shaped sub-vertical orebodies enveloped by hydrothermally altered rocks (Fig. 2a). Mineralized zones are associated with felsic subvolcanic rocks in the southern portion (Fig. 2b), whereas granitic-gneissic rocks are hosts in the northern portions (Fig. 2c). Outcrops are rare in the Jaguar deposit, thus a significant portion of the geological background is supported by drill core information. The lens-

shaped orebodies, up to 2 km long with variable width (up to 80 m), are concordant with the WNW regional structures, and commonly display a gradational contact with host rocks, characterized by the increasing abundance of hydrothermal minerals. It is noteworthy that fragments of granitic intrusions and felsic subvolcanic rocks are frequent in the hydrothermally altered rocks surrounding the deposit. Fragments of mafic–ultramafic rocks consist of altered diabase and ultramafic rocks, with the later predominating in the northern portion of the deposit, near the contact with the Serra do Puma layered intrusion.

3.1. Host rocks

The felsic subvolcanic rocks found in the southern portion of the deposit are massive, dark grey and porphyritic with abundant plagioclase and blue quartz phenocrysts within a fine-grained matrix of quartz, plagioclase, biotite and amphibole (Fig. 3a). Granitic rocks found in the northern portions are light grey, medium to coarse-grained massive rocks with tonalitic compositions. They consist of quartz, plagioclase, biotite and minor potassic feldspar and magnetite. In both host rocks, the presence of biotite and chlorite become abundant close to the mineralized zones, displaying millimeter-sized alteration patches (Fig. 3b) up to strongly foliated zones, a few meters wide. These occurrence of magnetite in the host rocks is constrained to these discrete alteration patches, and always associated with biotite and chlorite (Fig. 3c), not occurring in the matrix together with igneous minerals. The BIF from the Serra Arqueada consists of a fine alternation of magnetite- and quartz-rich layers (Fig. 3c), with subordinate biotite and muscovite. Host rocks also include two distinct sets of mafic dikes comprising an older and a younger generation. Both generations are dark grey and moderately magnetic, displaying millimeter-sized skeletal magnetite phenocrysts, with no ilmenite exsolution lamellae (Fig. 3d), within a fine-grained intergranular matrix.

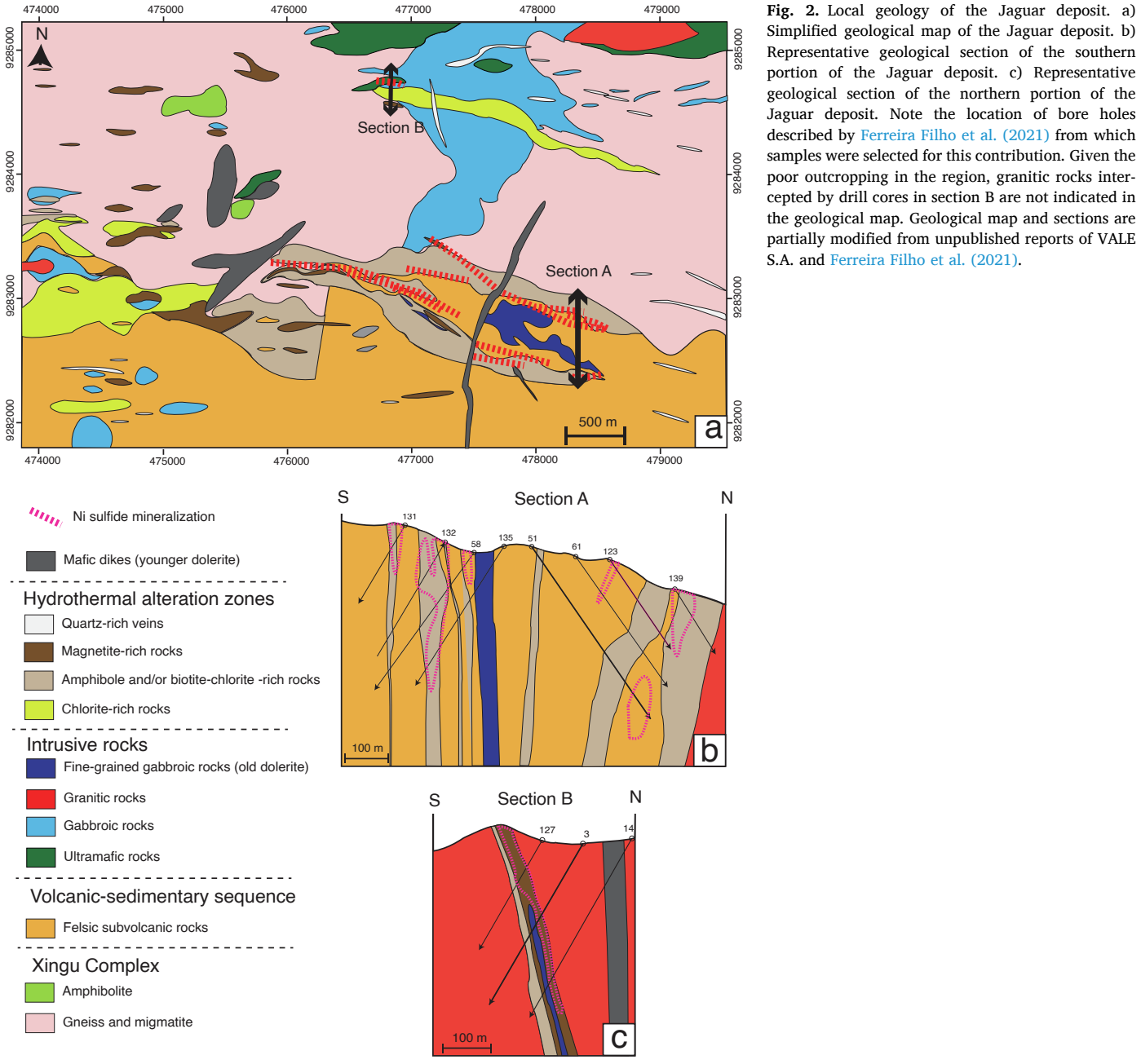

Fig. 2. Local geology of the Jaguar deposit. a) Simplified geological map of the Jaguar deposit. b) Representative geological section of the southern portion of the Jaguar deposit. c) Representative geological section of the northern portion of the Jaguar deposit. Note the location of bore holes described by Ferreira Filho et al. (2021) from which samples were selected for this contribution. Given the poor outcropping in the region, granitic rocks intercepted by drill cores in section B are not indicated in the geological map. Geological map and sections are partially modified from unpublished reports of VALE S.A. and Ferreira Filho et al. (2021).

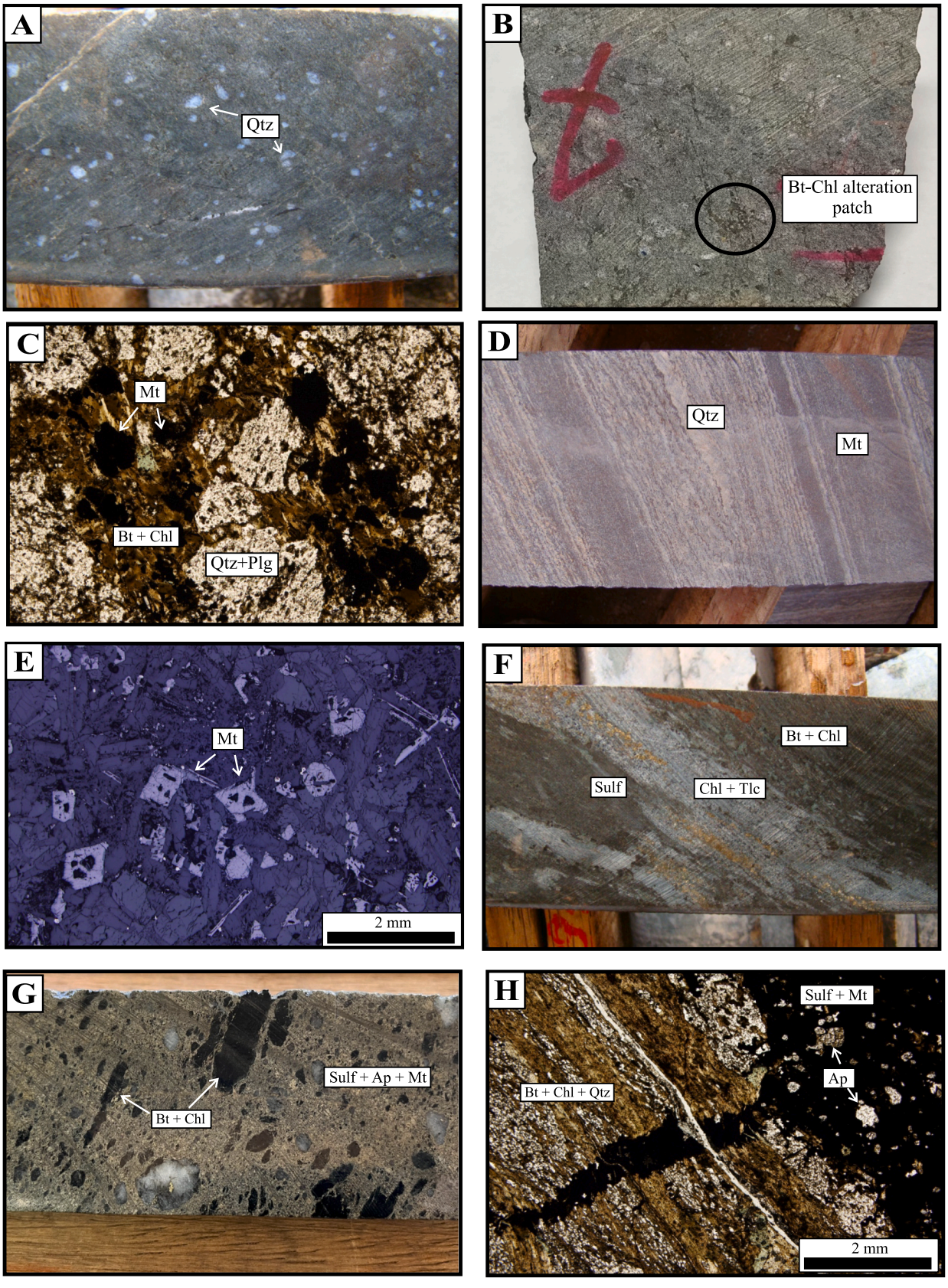

(caption on next page)

Fig. 3. Representative photos and photomicrographs of the main lithologies occurring at the Jaguar Deposit. A) Subvolcanic felsic rock with blue quartz crystals. B) Subvolcanic felsic rock displaying millimetre-sized Bt-Chl alteration patches containing disseminated magnetite. The alteration patch is highlighted by the black circle. C) Photomicrograph of Bt-Chl alteration patch with disseminated magnetite grains within a quartz- and plagioclase-dominated matrix of medium-grained tonalite. D) Finely layered banded iron formation (BIF) from Serra Arqueada Deposit. E) Photomicrograph of late mafic dyke that crosscuts the Jaguar deposit. Note the occurrence of euhedral magnetite crystals with slightly skeletal shape indicative of rapid cooling. F) Core sample of felsic subvolcanic rock extensively altered to biotite and chlorite, with fine sulfide veinlets. Note that biotite-chlorite alteration is superimposed by talc-chlorite alteration. G) Core sample of brecciated mineralization comprising sulfides, magnetite and apatite. Note that massive sulfide assemblage is late relative to biotite-chlorite alteration, which is locally observed as minor xenoliths. H) Photomicrograph of sulfide-magnetite-apatite veinlet crosscutting biotite-chlorite-rich rock. Act, actinolite; Ap, apatite; Bt, biotite; Chl, chlorite; Mt, magnetite; Plg, plagioclase; Qtz, quartz; Sulf, sulfides; Tlc, talc. (For interpretation of the references to color in this figure legend, the reader is referred to the web version of this article.)

3.2. Hydrothermal alteration zones

Ferreira Filho et al. (2021) defined three main types of alteration zones in the Jaguar deposit: (a) biotite-chlorite (Bt-Chl) zone, (b) amphibole (actinolite)-biotite (Amph-Bt) zone and (c) magnetite-apatite (Mt-Ap) zone. The Ni mineralization is mainly associated with the latter Mt-Ap zones. These alteration zones display a complex crosscutting relationship and vary in proportion and size at different portions of the deposit. For instance, alteration zones may develop from millimetre-sized discrete veinlets within the host rocks to corridors a few hundred-meters wide. The Bt-Chl zones define an early alteration varying from minor to moderate replacement (~30 vol%) of the host rocks up to completely altered bodies. The alteration consists of a fine-grained intergrowth of biotite and chlorite, typically defining mylonitic foliated bands alternating with fine-grained quartz- and plagioclase-rich bands (Fig. 3e). Chlorite occurs both in equilibrium with biotite and replacing it together with talc and quartz (Fig. 3e). The Amph-Bt alteration is scarcer and defines discontinuous lenses within both Bt-Chl and Mt-Ap alteration zones. The Mt-Ap alteration zones consist of medium-grained subhedral apatite and magnetite with associated fine-grained granular quartz. No exsolutions are observed in magnetite, which normally occurs as texturally homogeneous crystals. They are associated with the highest Ni sulfide ore grades in the Jaguar deposit. This alteration displays clear crosscutting relationships, whereby brecciated rocks overprint earlier biotite-chlorite and amphibole-biotite assemblages. In some places, fragments of the Bt-Chl alteration are found within the Mt-Ap breccias (Fig. 3f and 3 g), whereas in other cases the crosscutting relation is observed at a very small scale (Fig. 3h).

3.3. Ni mineralization

Two main types of Ni sulfide mineralization, referred to as Type I and Type II, were described by Ferreira Filho et al. (2021) in the Jaguar deposit. Type I mineralization is the most abundant and yields the lower Ni grades found in the deposit. This mineralization style is mainly hosted within the Bt-Chl alteration zones and consists of sulfide-bearing veinlets developed parallel to the main foliation, with no consistent association with magnetite or apatite (Fig. 3e). However, local discordant fractures and veins with disseminated sulfides are also observed. Type II mineralization is less abundant but yields the highest grades and is associated with the Mt-Ap alteration. It occurs as brecciated bodies with irregular fragments of extensively altered host rocks within a sulfide-, magnetite-, and apatite-rich matrix (Fig. 3f and 3 g). Mineralized breccias occur in up to 80 m thick zones, frequently parallel to or crosscutting Bt-Chl alteration zones at a low angle (Fig. 2b and 2c). In a recent contribution, Ferreira Filho et al. (2021) argued that the Bt-Chl alteration zones represent extensive early alteration zones that are further overprinted by the Mt-Ap alteration, likely supporting different pulses of hydrothermal fluid flow.

The sulfide assemblages in both ore types (i.e., Type I and Type II) consist mainly of pyrite and millerite, closely associated with magnetite, apatite and quartz (Fig. 4a and 4b). Although there is variation in the relative abundance of BMS in the deposit, pyrite and millerite are the most common sulfide minerals. Magnetite is normally euhedral and is surrounded by sulfides. Locally, sulfide veinlets crosscut magnetite, which support that sulfide formation is slightly later than magnetite (Fig. 4). Nevertheless, both phases display a systematic spatial association, and sulfide-rich zones without magnetite are rare (mostly in Type I mineralization). Pyrite occurs mostly as euhedral to subhedral crystals (pyrite-I) but may form irregular anhedral aggregates (pyrite-II) within other sulfides (Fig. 4c). In the former, magnetite inclusions are frequently observed within pyrite, whereas the latter supports the recrystallization of previously formed sulfides. Millerite mainly occurs as fine-grained intergranular network enclosing euhedral pyrite grains or aggregates and is locally altered to polydymite or violarite (Fig. 4d). Variable, but usually minor relative to other sulfide minerals, pentlandite, chalcopyrite and pyrrhotite are also observed (Fig. 4e and 4f). Although restricted to a few localities, the assemblage of pyrite, pyrrhotite, pentlandite and chalcopyrite with magnetite and apatite is also observed (Fig. 4g). Moreover, very fine-grained pentlandite flame exsolutions in pyrrhotite may also be found in these cases (Fig. 4h). Restricted to few parts of the deposit, sphalerite occurs within the sulfide-rich matrix and displays fine-grained aligned inclusions of chalcopyrite.

4. Methodology

4.1. Sample selection

Thirty-six well-characterized samples were chosen from the detailed study of Ferreira Filho et al. (2021) to reflect the representative variations found in host rocks (felsic subvolcanic and granitic rocks, n = 6) and different alteration styles (Bt-Chl, n = 10 and Mt-Ap, n = 12) of mineralized horizons. Additional samples of banded iron formation (BIF) from the Serra Arqueada (n = 2) and the younger generation of mafic dykes (n = 2) were selected to provide a comparison of the results with surrounding oxide-bearing lithologies that are presumably unrelated to the Ni mineralization (Oliveira, 2017; Ferreira Filho et al., 2021).

4.2. Laser ablation-inductively coupled plasma mass spectrometry

The concentration and distribution of the minor and trace elements were determined by laser ablation-inductively coupled plasma-mass spectrometry (LA-ICP-MS) at LabMaTer, Université du Québec à Chicoutimi (UQAC), using an Excimer 193 nm RESOlution M−50 laser ablation system (Australian Scientific Instrument) equipped with a double volume cell S-155 (Laurin Technic), and coupled with an Agilent 7900 ICP-MS. The LA-ICP-MS parameters were a laser frequency of 10 Hz, a power of 3–5 mJ/pulse, a dwell time of 7.5 ms, a rastering speed of 5–10 μm/s, and a fluence of 3–5 J/cm^2. Line scans across the surface of grains were made with beam sizes of 55 and 44 μm, depending on grain size. The gas blank was measured for 30 s before switching on the laser for at least 60 s. The ablated material was carried into the ICP-MS by an Ar–He gas mix at a rate of 0.8–1 L/min for Ar and 350 mL/min for He, and 2 mL/ min of nitrogen was also added to the mixture. Data reduction was carried out using the Iolite package for Igor Pro software (Paton et al., 2011).

^{57}Fe was used for internal standardization of sulfide minerals (pyrite,

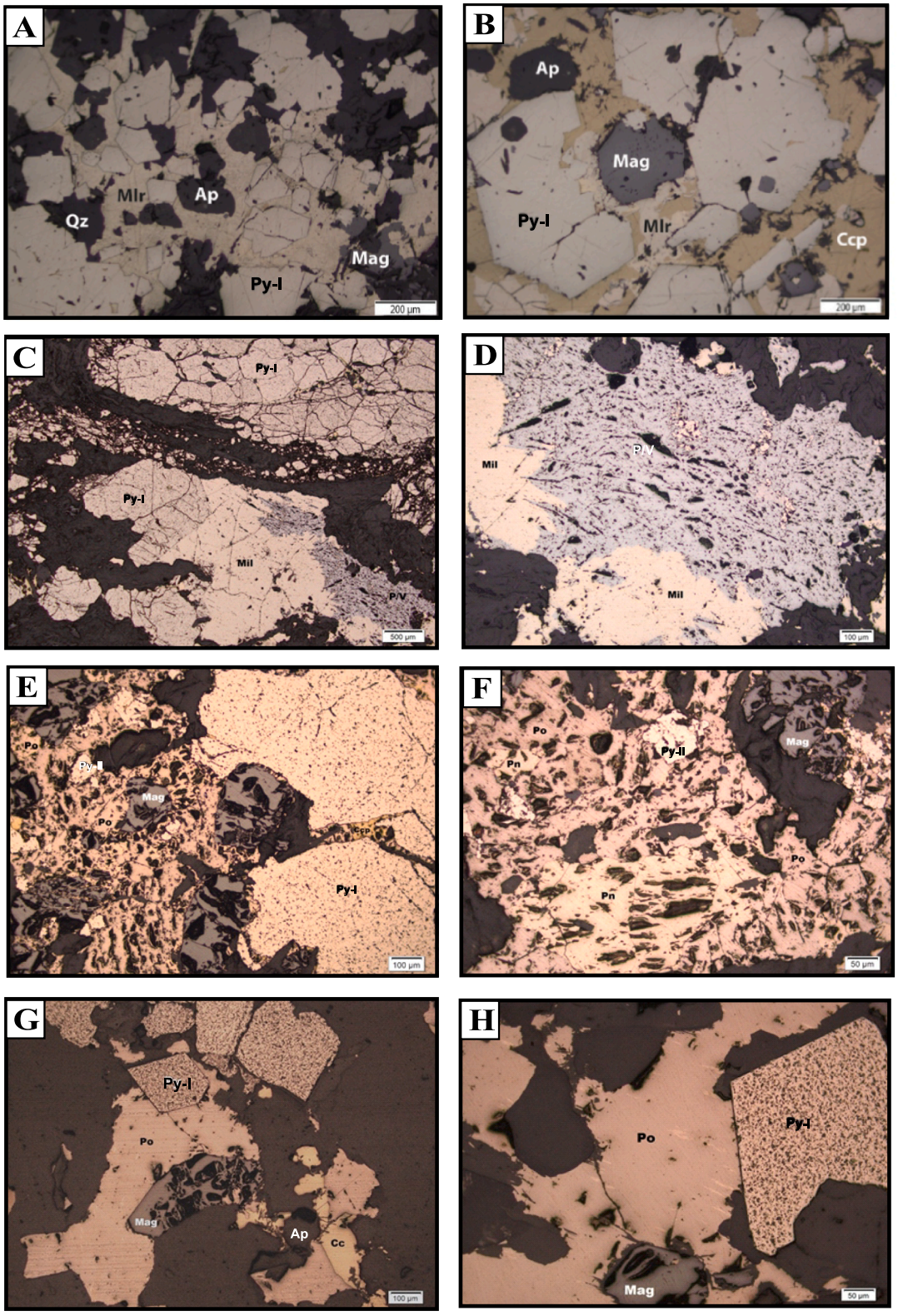

Fig. 4. Representative reflected light photomicrographs of the ores from the Jaguar Deposit. A) Euhedral pyrite grains within millerite matrix. Note the association with quatz, apatite and magnetite. B) Euhedral pyrite and magnetite grains included within chalcopyrite-dominated matrix. Round-shaped apatite grain is also observed included in chalcopyrite. C) Pyrite and millerite with fine-grained pervasive polydymite/violarite (P/V) alteration. D) Polydymite/violarite (P/V) alteration and millerite grains associated with apatite. E) Large euhedral pyrite grains with small chalcopyrite association, together with magnetite and apatite grains included in anhedral pyrrhotite matrix. F) Pentlandite- and pyrrhotite-dominated sulfide assemblage with minor pyrite inclusions, together with anhedral magnetite grain. G) Euhedral pyrite and magnetite grains associated with pyrrhotite and chalcopyrite. H) Large euhredral pyrite grain associated with pyrrhotite crystal displaying fine-grained pentlandite exsolution lamellae. Note the magnetite grain included within pyrrhotite. Ap, apatite; Ccp, chalcopyrite; Mag, magnetite; Mil, millerite, Qtz, quartz; Pn, pentlandite; Po, pyrrhotite; Py, pyrite.

millerite, chalcopyrite, pentlandite, pyrrhotite and sphalerite) using values reported by Oliveira (2017). Calibration followed that described in Mansur et al. (2021a). Three certified reference materials were used for external calibration of sulfide minerals: Laflamme Po727, which is a synthetic FeS doped with ~ 40 ppm PGE and Au supplied by Memorial University of Newfoundland, was used to calibrate for PGE, Au and S; MASS-1, which is a ZnCuFeS pressed powder pellet doped with 50–70 ppm of most chalcophile elements, supplied by the United States Geological Survey (USGS), was used to calibrate for Co, Cu, Zn, Ga, Ge, As, Se, Mo, Ag, Cd, Sn, Sb, Te, Tl, Pb and Bi; GSE-1 g, which is a natural basaltic glass fused and doped with most elements at 300–500 ppm, supplied by the USGS, was used to calibrate for Ti, Ni, In, and Re using preferred values from the GeoReM database (Jochum et al., 2005). MASS-1, GSE1g, JB-MSS-5 (an FeS sulfide containing 50–70 ppm of most chalcophile elements, supplied by James Brenan) and UQAC-FeS1 (a synthetic sulfide developed at LabMaTer) were used to monitor the results. The results obtained were generally in good agreement with the working values (ESM - Table A1). Polyatomic interference of $^{63}Cu^{40}Ar$ on ^{103}Rh was corrected using ^{103}Rh measured in MASS-1, which contains 13.4 % Cu but no Rh. One percent Cu produced ~ 0.1 ppm interference. Thus, the ^{103}Rh values in chalcopyrite are not reported as the interference is too large to be corrected. Direct interferences of ^{108}Cd on ^{108}Pd and ^{115}Sn on ^{115}In were corrected by monitoring ^{111}Cd and ^{118}Sn, respectively. Interference of $^{68}Zn^{40}Ar$ on ^{108}Pd is negligible as Zn is present mostly at < 1000 ppm. Polyatomic interference of $^{61}Ni^{40}Ar$ on ^{101}Ru was corrected using ^{101}Ru measured in a NiS blank, which does not contain Ru. One percent Ni produced ~ 0.007 ppm interference and was not significant a significant part of the Ru signal.

For magnetite analyses the internal standardization was also based on ^{57}Fe using values previously obtained by electron microprobe (Oliveira 2017) in the same samples. Calibration followed that described in Dare et al. (2014). Silicate, apatite and sulfide inclusions encountered during laser ablation were excluded from the signal during data reduction. GSE-1 g was used to calibrate for all elements using preferred values from the GeoReM database (Jochum et al., 2005). In addition, GSD-1 g and G-probe 6, which are respectively a synthetic glass and a natural basalt glass (both supplied by the USGS), and BC28, which is a natural magnetite from the Main Magnetite layer of the Bushveld Complex (supplied by LabMaTer), were used as quality control reference materials to monitor the calibration of GSE-1 g. Following Dare et al. (2012), polyatomic interferences of ^{90}Zr from $^{50}Ti^{40}Ar$, $^{50}V^{40}Ar$, and $^{50}Cr^{40}Ar$; ^{92}Zr from $^{52}Cr^{40}Ar$; and ^{93}Nb from $^{53}Cr^{40}Ar$ are considered negligible in magnetite, and corrections are not required. The results obtained were generally in good agreement with the working values (ESM - Table A1).

Maps of element distribution were made on different sulfide assemblages using a laser frequency of 15 Hz and a power of 5 mJ/pulse. The beam size (33–44 μm) and the stage movement speed (10–15 μm/s) were adapted to optimize spatial resolution and analysis time for grains of different sizes. The maps were generated using the Iolite software package based on the time-resolved composition of each element. The maps indicate the relative concentration of the elements and are semi-quantitative.

5. Results

5.1. Distribution of chalcophile elements among the base metal sulfides

Compositional LA-ICP-MS maps for different mineral assemblages from Type II ore (sulfide-magnetite-apatite assemblage) of the Jaguar deposit are shown in Figs. 5 and 6. Fig. 5 shows the distribution of trace elements in Type II ore containing a euhedral pyrite grain (pyrite-I) within a pentlandite-millerite, magnetite, and apatite matrix. The compositional maps reveal the preference of Ti, V and Ga into magnetite. Fig. 6 represents a pyrrhotite, pentlandite and chalcopyrite assemblage in the less common Type I ore (sulfide only assemblage). There is much variation in the relative abundance of BMS at different portions of the deposit (Ferreira Filho et al., 2021), and although the concentration of trace elements is also variable, their distribution among the different BMS is similar among the different alteration facies. The range of concentrations of trace elements in chalcopyrite, millerite, pentlandite, pyrite-I, pyrite-II, pyrrhotite and sphalerite from the Jaguar deposit are shown in Fig. 7, and the complete data set (individual analyses) is provided in the Electronic Supplementary Materials (ESM – Table A2 to A7). The minerals were not separated according to their different alteration facies here as there is much overlap and no systematic difference was observed. Therefore, analyses of BMS hosted within both Bt-Chl and Mt-Ap alterations were grouped for simplicity. Despite the wide variation in the composition of each BMS, Fig. 7 illustrates the preference of each element for different BMS and their concentration ranges.

The LA-ICP-MS compositional maps show that most chalcophile elements display a homogeneous distribution in BMS, except for Co, As, and to a lesser extent Se, which display a strong oscillatory zoning in pyrite (Fig. 5). Cobalt and As are more concentrated in euhedral pyrite (pyrite-I), with concentrations ranging from 1000 to 10000 ppm (Fig. 7a) and 100 to 1000 ppm, respectively. Relatively higher concentrations of Co are also observed in millerite, pentlandite and sphalerite, ranging mainly from 100 to 1000 ppm, whereas<10 ppm in chalcopyrite and pyrrhotite. Although Se concentrations range mainly from 10 to 100 ppm in all BMS, the highest concentrations are found in millerite. Relative to pyrite-I, pyrite-II yields lower concentrations of As (1 to 10 ppm versus 100 to 1000 ppm), but higher Ag (1 to 10 ppm versus < 1 ppm), Au (0.1 to 1 ppm versus < 0.01 ppm), Bi (10 to 1000 ppm versus 0.1 to 10 ppm), Sb (0.1 to 10 ppm versus < 0.1 ppm), Pb (10 to 100 ppm versus 0.1 to 10 ppm), Te (1 to 10 ppm versus < 3 ppm) and Tl (0.1 to 1 ppm versus < 0.01 ppm) concentrations (Fig. 7). Apart from pyrite-II, Au, Bi, Sb and Pb are equally distributed among the remaining BMS, ranging from 1 to 20 ppm for Bi and Pb, and mostly below 0.1 ppm for Au and Sb.

Millerite and pentlandite have the highest Ni contents, as expected, but also yield high concentrations of Te at around 10 ppm. Apart from chalcopyrite, Cu values range mainly from 10 to 1000 ppm in all the other BMS, with a significant overlap among them. Moreover, chalcopyrite also hosts the highest concentrations of Sn, ranging from 0.1 to 1 ppm, and together with sphalerite, high In contents in the 0.1 to 10 ppm range. In addition to Zn, sphalerite hosts the highest Cd concentrations, dominantly higher than 1000 ppm, followed by chalcopyrite in the 0.1 to 10 ppm range, whereas all the remaining BMS have contents below 1 ppm. Palladium concentrations are mostly below detection limit in all BMS (i.e. below 0.1 ppm), apart from pentlandite, in which concentrations range from 0.1 to 1 ppm. Molybdenum and Re concentrations are similar among all BMS, and mainly lower than 1 ppm. Although LA-ICP-MS compositional maps reveal homogeneous distribution of Ti, Ga, V and Ge at low levels in pentlandite and chalcopyrite (i.e. below 1 ppm), their concentrations in most individual analyses are below detection limits.

5.2. Trace elements in magnetite

The compositional ranges for magnetite from different rock types are illustrated in box and whisker diagrams in Fig. 8. The samples were divided into the BIF from Serra Arqueada, the younger dolerite generation (i.e. mafic dyke), felsic subvolcanic and granitic host rocks, and Bt-Chl and Mt-Ap alteration facies of the mineralized horizon. Most trace elements show several orders of magnitude variations in magnetite, but the compositional ranges differ among the different rock types. The complete data set (individual analyses) is provided in the Electronic Supplementary Materials (ESM – Table A8).

Magnetite from mafic dykes is readily distinguished from magnetite from the other rock types (Fig. 8a to 8 h) by their higher concentrations of Ti (~10 wt%), V (2000 to 4000 ppm), Mn (~7000 ppm), Zr (200 to

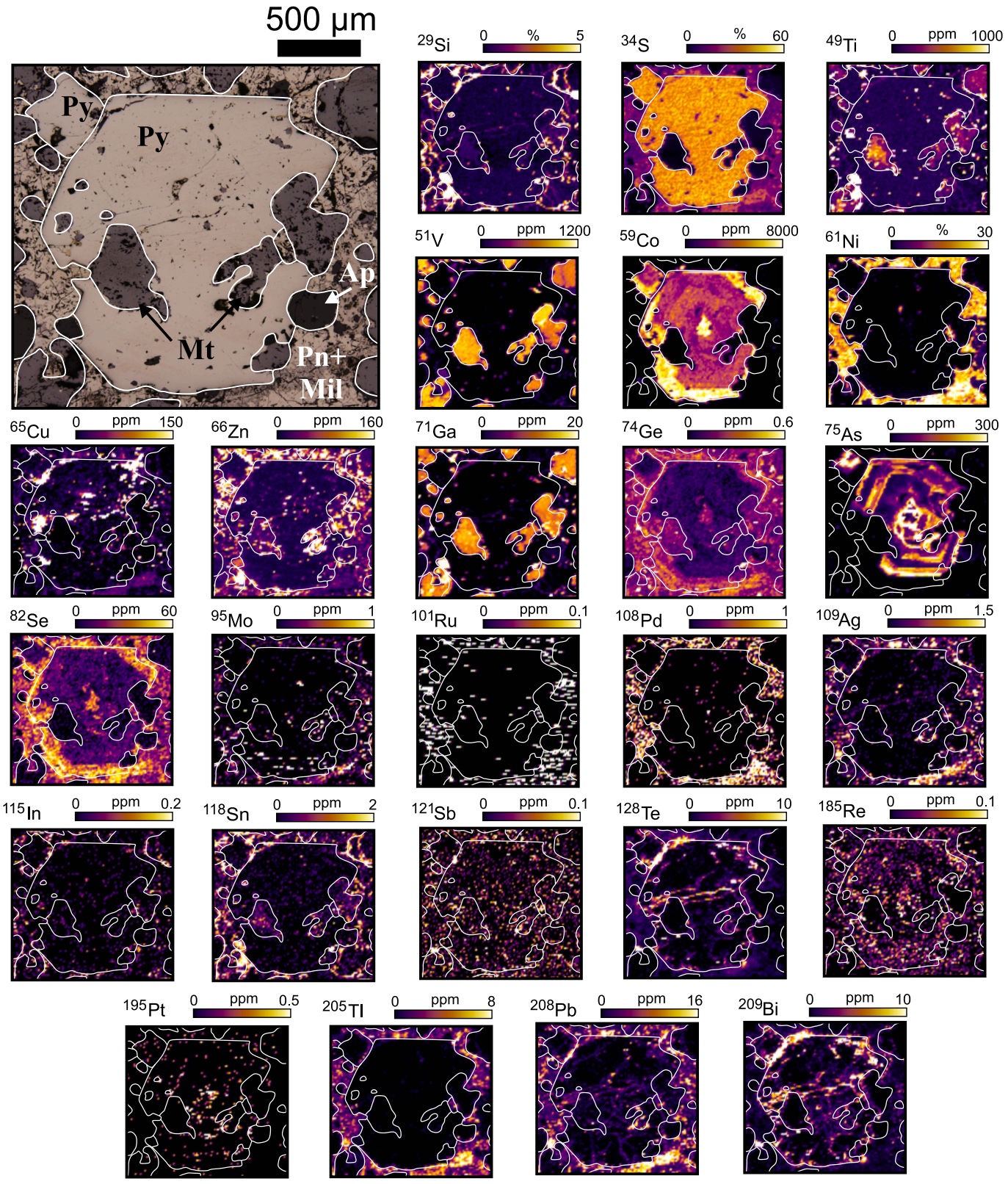

Fig. 5. LA–ICP-MS elemental maps showing the distribution of chalcophile elements in coarse-grained pyrite grain within fine-grained pentlandite and pyrrhotite matrix. Note rounded magnetite and apatite grains are included within sulfide minerals. White lines show the grain outlines. The relative concentrations of the elements are semi-quantitative. Ap, apatite; Mil, milerite; Mt, magnetite; Pn, pentlandite; Py, pyrite.

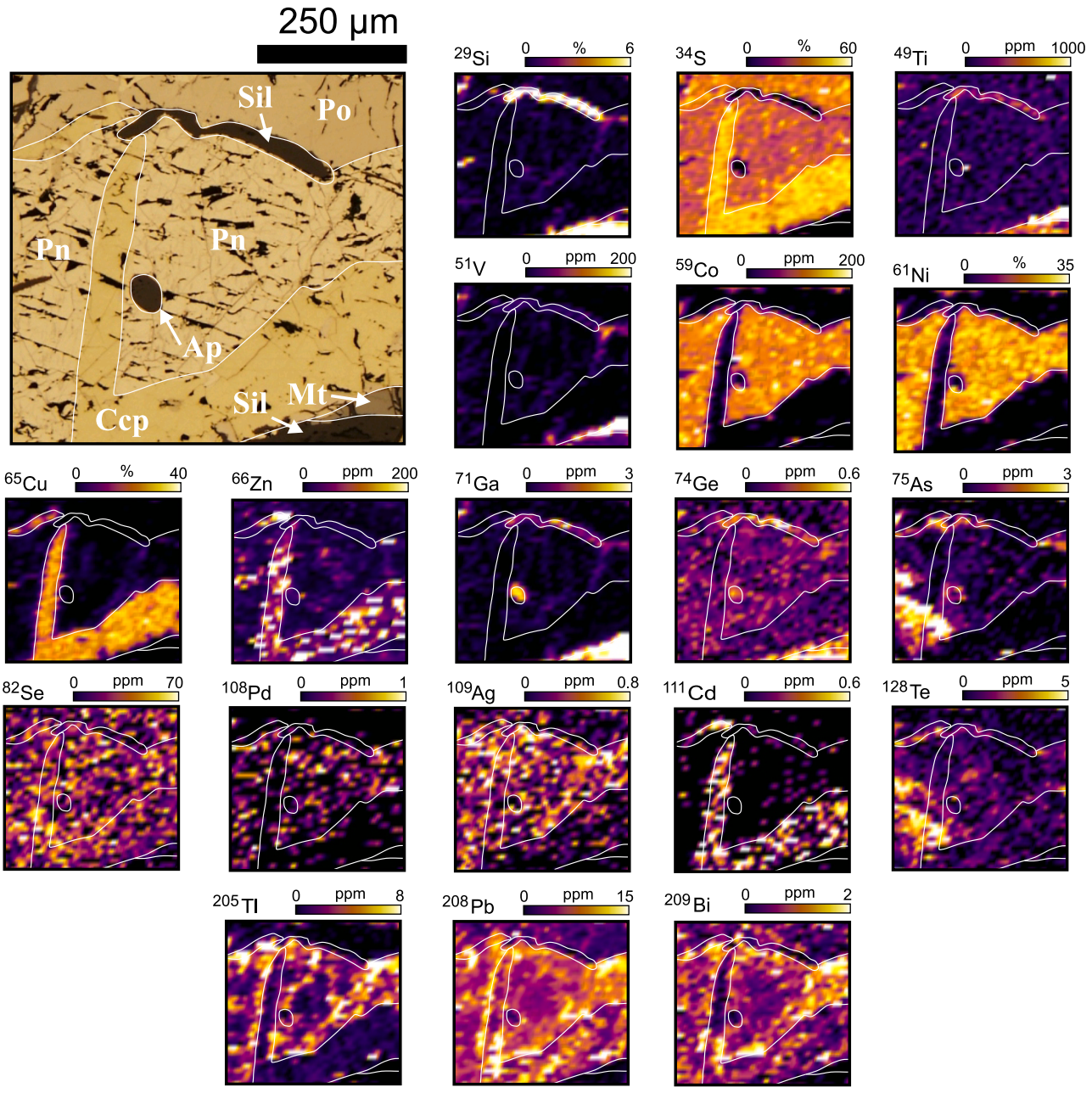

Fig. 6. LA–ICP-MS elemental maps showing the distribution of chalcophile elements in pyrrhotite, pentlandite and chalcopyrite. Note rounded apatite inclusion within pentlandite. White lines show the grain outlines. The relative concentrations of the elements are semi-quantitative. Ap, apatite; Ccp, chalcopyrite; Mt, magnetite; Pn, pentlandite; Po, pyrrhotite; Py, pyrite; Sil, silicate.

400 ppm), Al (~1 wt%), Zn (~1200 ppm), Ga (~40 ppm) and Hf (1 to 10 ppm), typical of igneous mafic rocks. The host rocks of Jaguar deposit (felsic subvolcanic rock and granites) also have higher concentrations of Ti (1000 to 50000 ppm versus 100 to 1000 ppm), Mn (300 to 5000 ppm versus 100 to 300 ppm), Zr (1 to 200 ppm versus 0.1 to 10 ppm), Al (700 to 7000 ppm versus 700 to 4000 ppm) and Hf (0.01 to 8 ppm versus 0.01 to 0.2 ppm) in magnetite relative to magnetite from the hydrothermal alteration facies (Bt-Chl and Mt-Ap zones). On the other hand, magnetite from host rocks and hydrothermal alteration facies has comparable V (200 to 1000 ppm), Zn (50 to 500 ppm) and Ga (5 to 50 ppm) concentrations.

Niobium (5 to 100 ppm) and Ta (0.5 to 10 ppm) concentrations are similar in magnetite from mafic dykes and host rocks, and higher than those found in the other rock types (Fig. 8i and 8j). Chromium concentrations (Fig. 8k) of magnetite from mafic dykes and the felsic host rocks are similar (50 to 500 ppm) and overlap with those from Bt-Chl alteration, which are higher than those from Mt-Ap alteration (1 to 10 ppm). Magnesium (Fig. 8l) and La (Fig. 8m) have a similar distribution and concentrations overlap among magnetite from different rock types (700 to 6000 ppm and 0.05 to 30 ppm, respectively). Although Ca concentrations (Fig. 8n) in magnetite of host rocks and hydrothermal facies (200 to 2000 ppm) are also similar, they are slightly higher than those from mafic dykes (100 to 500 ppm). Nickel (Fig. 8o) and Co (Fig. 8p) are evenly distributed, showing slightly higher concentrations in magnetite from both Bt-Chl and Mt-Ap alteration zones relative to those from felsic host rocks and mafic dykes (800 to 3000 ppm versus 500 to 700 ppm for Ni and 10 to 80 ppm versus 7 to 20 ppm for Co, respectively). Finally, the concentration of most trace elements in magnetite is remarkably lower in the Serra Arqueada BIF than in all the other rock types (Fig. 8). The exception is Ge (Fig. 8q), for which

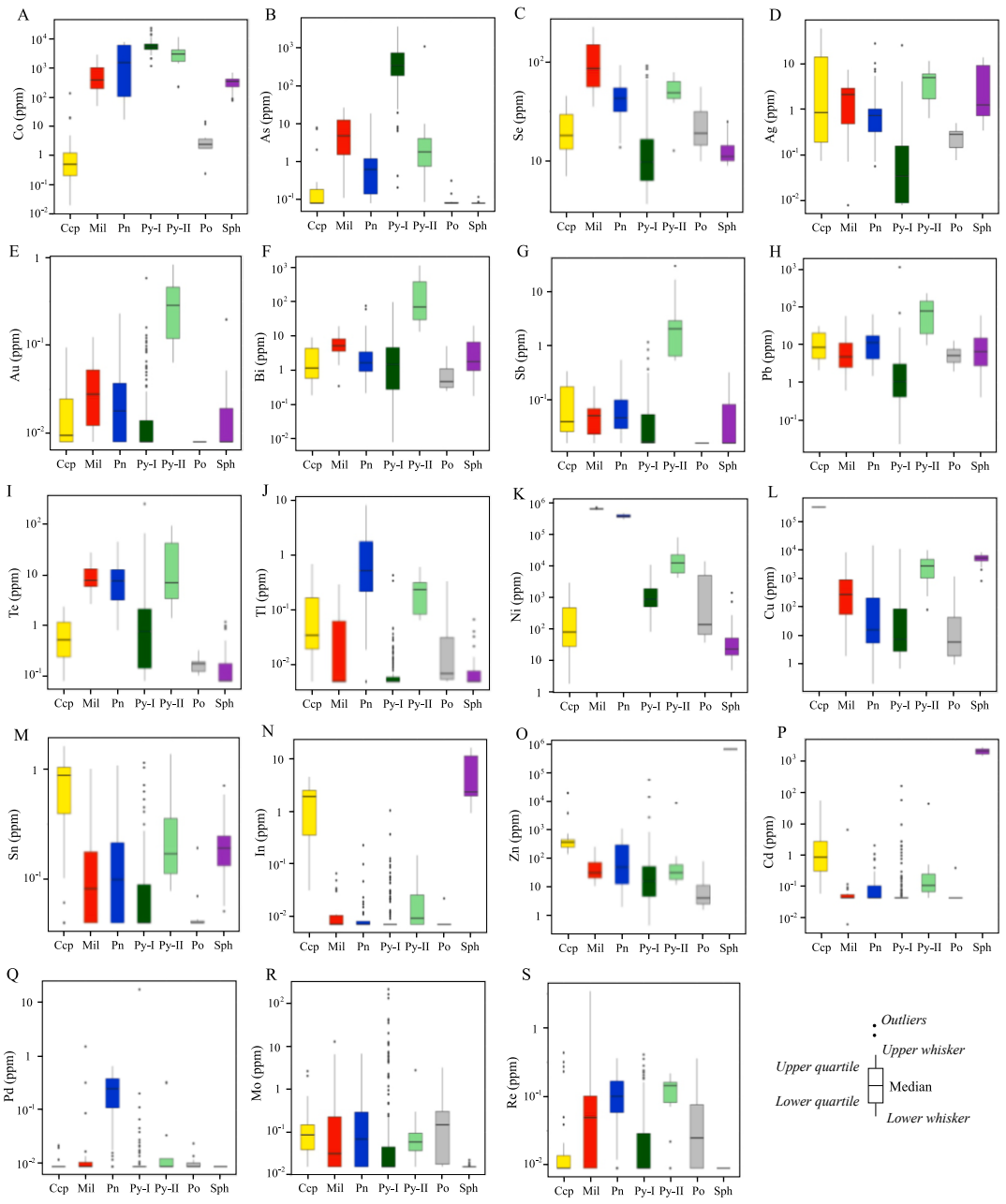

Fig. 7. Box and whisker diagrams of Ni (A), Co (B), As (C), Ag (D), Au (E), Bi (F), Sb (G), Pb (H), Te (I), Se (J), Tl (K), Pd (L), Cu (M), Zn (N), Cd (O), In (P), Sn (Q), Mo (R) and Re (S) concentrations in chalcopyrite (Ccp), millerite (Mil), pentlandite (Pn), pyrite-I (Py-I), pyrite-II (Py-II), pyrrhotite (Po) and sphalerite (Sph) from the Jaguar Deposit.

concentrations are higher in magnetite from BIF relative to others (7 to 30 ppm versus 0.5 to 2 ppm). Only Sn (Fig. 8r) and Pb (Fig. 8s) display comparable contents in magnetite from all rock types (0.1 to 20 ppm).

It has been shown that hydrothermal magnetite from distinct localities may display strong oscillatory zoning in major and trace elements (Dare et al., 2014, 2015; Nadoll et al., 2014; Huang and Beaudoin, 2019, 2021). Therefore, trace element compositional maps were performed in magnetite from the Jaguar deposit to assess the distribution of different elements. Fig. 9 shows the distribution of trace elements in magnetite grains from the Mt-Ap alteration facies of the Jaguar deposit. Although the distribution of most trace elements in magnetite is relatively homogeneous at the grain scale (Fig. 9), Ti, Mn and to a lesser extent V display a slightly core to rim zonation, with their concentrations becoming progressively lower towards the grain borders. Thus, no strong oscillatory zoning is observed in studied magnetite from our samples.

In order to compare large variations of the full suite of trace elements in magnetite from different rock types, we used the multi-element variation diagram proposed by Dare et al. (2014). The reasoning for the diagram is detailed by the authors and only a summary is provided here. The elements are normalized to Bulk Continental Crust (CC) composition (Rudnick et al., 2003) and plotted in order of progressively increasing compatibility with magnetite in silicate systems. Therefore, the most compatible elements in magnetite are plotted on the right-side of the diagram, whereas the least compatible elements are placed on the left side. These plots readily allow the assessment of major variations in magnetite composition and provide a simultaneous display of a wide range of trace elements. Fig. 10 shows the median concentration of magnetite for each sample and each rock type (black lines) plotted in multi-element diagrams. The rock classification follows that presented

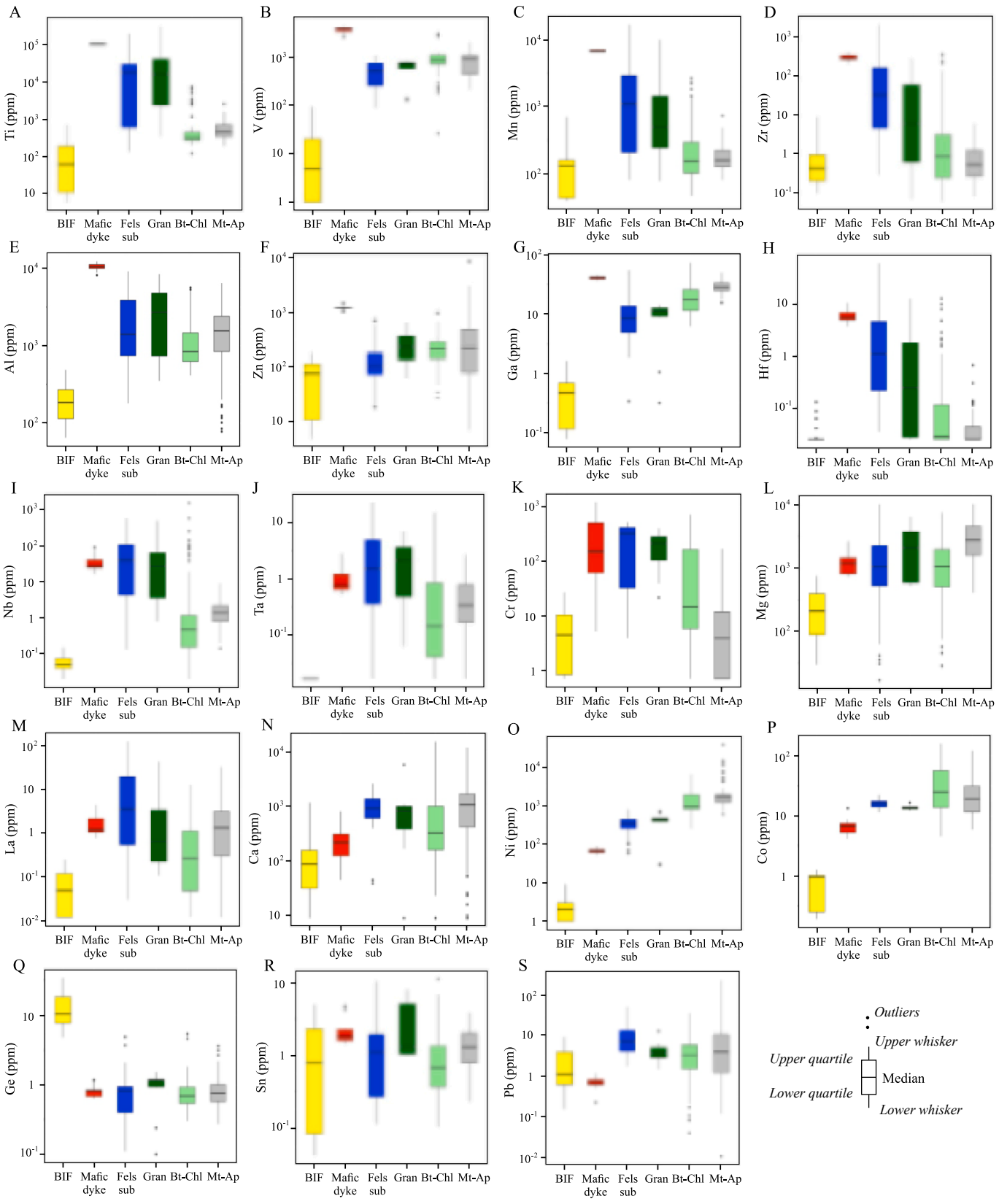

Fig. 8. Box and whisker diagrams of Ti (A), V (B), Mn (C), Zr (D), Al (E), Zn (F), Ga (G), Nb (H), Ta (I), Hf (J), Mg (K), Cr (L), La (M), Ni (N), Co (O), Ca (P), Ge (Q), Sn (R) and Pb (S) concentrations in oxides from the banded iron formation (BIF), mafic dyke felsic subvolcanic rock (Fels sub), granite (Gran), biotite-chlorite alteration (Bt-Chl) and magnetite-apatite alteration (Mt-Ap) from the Jaguar Deposit.

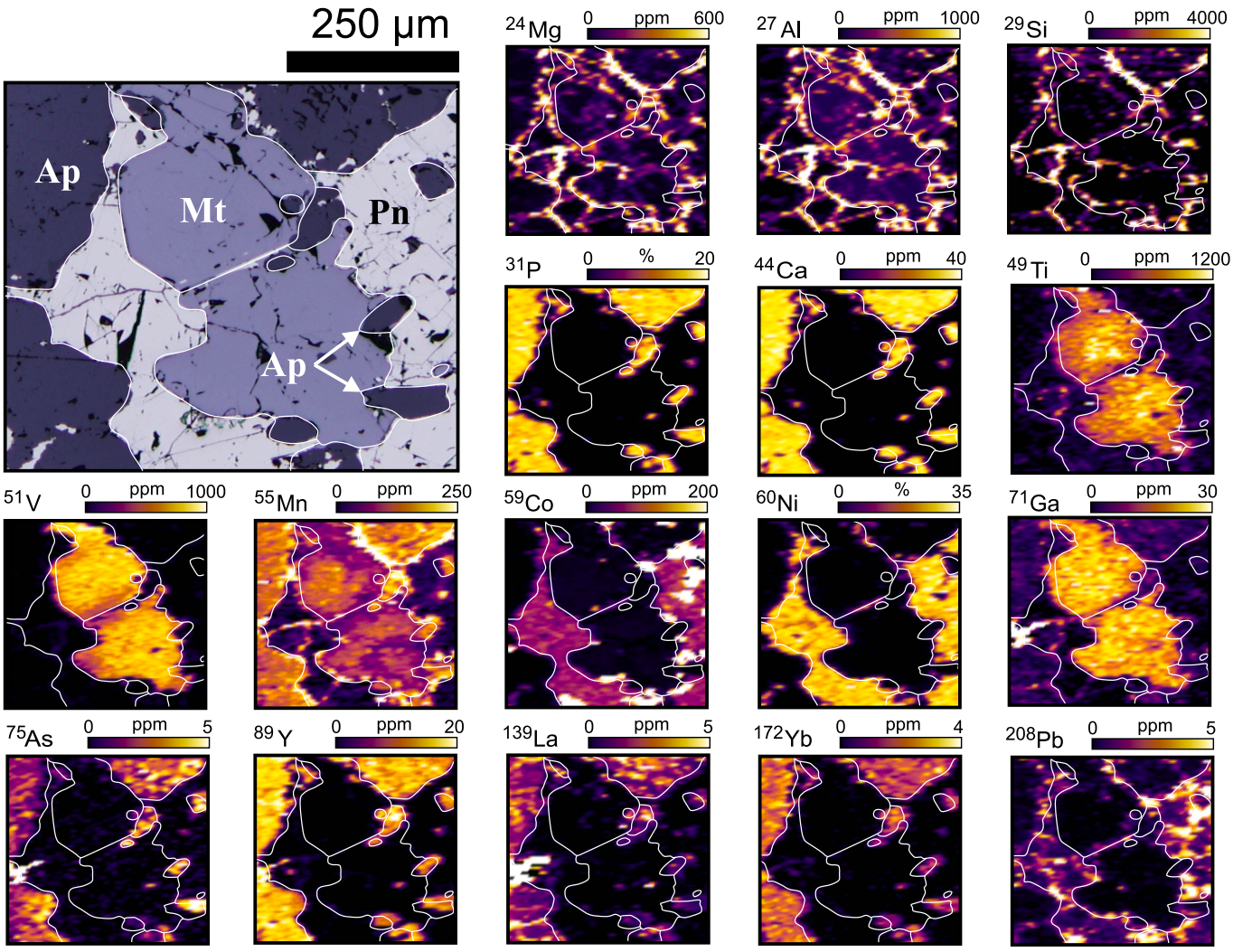

Fig. 9. LA–ICP-MS elemental maps showing the distribution of trace elements in magnetite grains associated with apatite and pentlandite. Note that magnetite, apatite and pentlandite are in textural equilibrium. White lines show the grain outlines. The relative concentrations of the elements are semi-quantitative. Ap, apatite; Mt, magnetite; Pn, pentlandite.

in the box and whisker diagrams (Fig. 8).

Magnetite from the younger generation of mafic dykes yield a pattern with positive slope varying from 0.01 to 1 times CC for least compatible elements such as Si and Pb, until 1 to 20 times CC for more compatible elements such as Ti and V (Fig. 10a), with negative Mg and Co anomalies, at around 0.1 to 1 times CC. The pattern displayed by magnetite from the younger mafic dyke generation is very similar to those for magnetite from evolved mafic rocks reported by Dare et al. (2014), with similar Ni-Cr normalised values. Magnetite from the felsic host rocks (subvolcanic rock and granites) also display a positive slope from least to more compatible elements (Fig. 10b). However, magnetite from the granites has slightly lower concentrations of most elements compared to those from the felsic subvolcanic rock. The magnetite pattern of the felsic host rocks most resembles that of mafic dykes, but with some differences such as much higher Ni than Cr (i.e., lower Ni/Cr ratios) in the former relative to the latter. In addition, magnetite from the felsic host rocks has higher Nb, Ta and W. It is noteworthy that, as previously described, magnetite from the felsic host rocks does not occur in clear association with the igneous minerals but is rather associated with biotite and chlorite in discrete alteration pockets. Typical igneous magnetite from felsic rocks is also shown in Fig. 10b, and it is clearly different from magnetite in the host felsic rocks at Jaguar, which is constrained to discrete Bt-Chl alteration patches (Fig. 3b and 3c).

The multi-element patterns for magnetite from Bt-Chl (Fig. 10c) and Mt-Ap (Fig. 10d) alteration facies of the mineralized zone are comparable. In both cases the patterns display a slightly positive slope varying from 0.01 to 1 times CC for the least compatible elements, such as Si and Pb, up to 10 to 100 times CC for more the compatible elements, such as Zn and V. The patterns also display slightly positive Pb, Ge, W and Zn anomalies, and remarkably negative Cr anomalies relative to Ni. Similar patterns, especially displaying a strong negative Cr anomaly relative to Ni (i.e. high Ni/Cr ratios) are typically characteristic of magnetite from different hydrothermal systems as argued by Dare et al. (2014). Nevertheless, it is noteworthy that magnetite from both hydrothermal alteration facies yield very high Ni values ranging from 10 to 300 times CC (Fig. 10c and 10d). Magnetite from the Serra Arqueada BIF has low concentrations of most trace elements and display relatively flat multi-element patterns (Fig. 10e), typical of low temperature magnetite from BIF environments. Most elements vary from 0.1 to 1 times CC, with positive Pb, Ge, Sn, Mn and Zn anomalies ranging from 1 to 10 times CC.

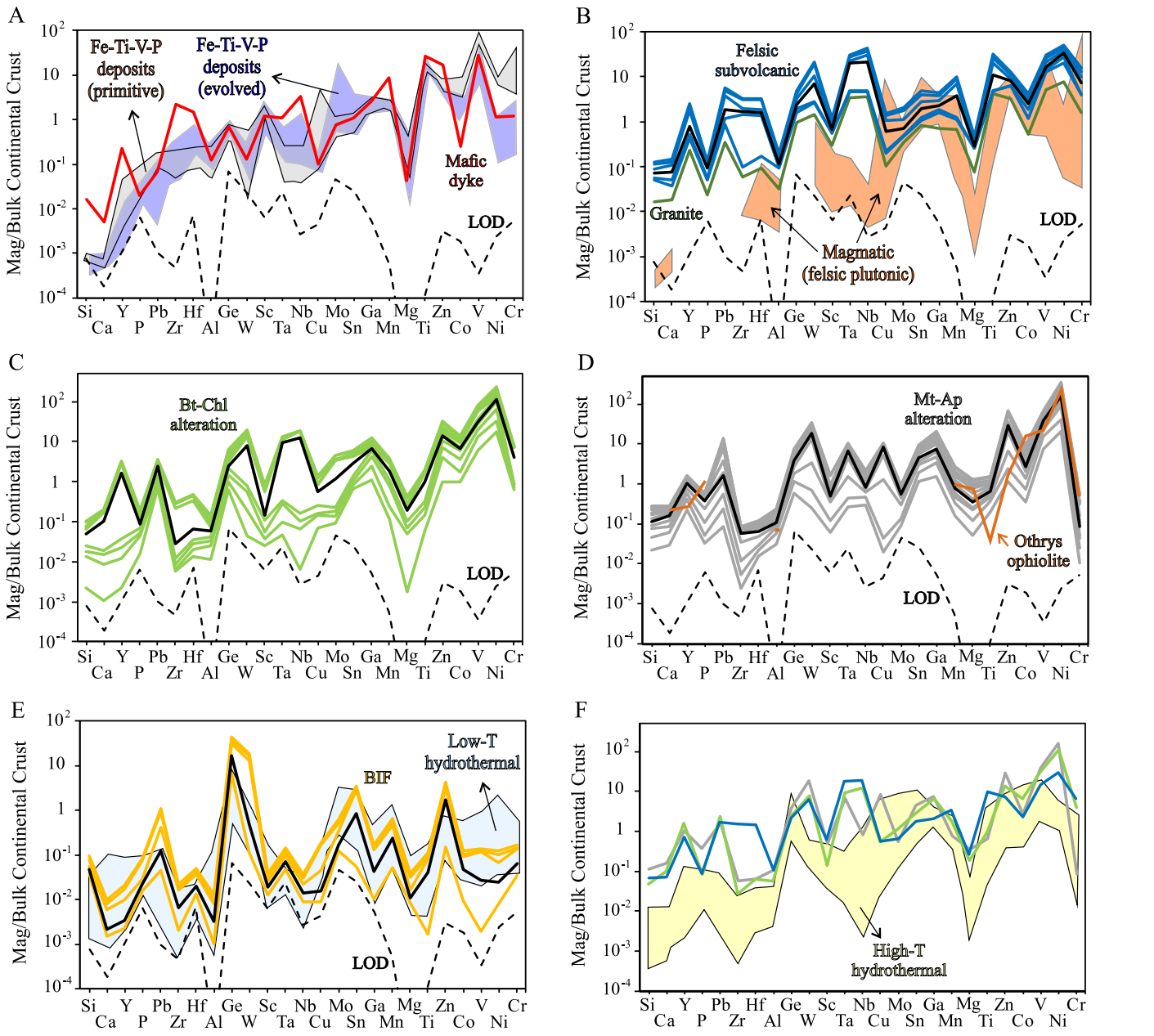

Fig. 10. Bulk continental crust-normalized multielement diagram of magnetite from (A) mafic dyke, (B) felsic subvolcanic and granite, (C) Bt-Chl alteration, (D) Mt-Ap alteration and (E) BIF from the Jaguar Deposit area. Each line represents the median value for an individual sample and black full lines are the median values for each rock type. Average composition of magnetite from Othrys ophiolite reported by Mitsis and Economou-Eliopoulos (2001 and 2003) is shown for reference in (D). The compositional fields for magnetite from high- and low-temperature hydrothermal and Fe-Ti-V-P deposits (primitive and evolved), and felsic plutonic rocks from Dare et al. (2014) are shown for reference. Median values for host rocks, Bt-Chl alteration and Mt-Ap alteration from the Jaguar Deposit (same color as in B, C and D) and compositional field for high-temperature hydrothermal magnetite are shown in (F). Bulk continental crust values from Rudnick and Gao (2003), and order of elements with increasing compatibility with magnetite to the right (after Dare et al. 2014). Dashed black lines represent the limit of detection (LOD) for different elements.

6. Discussion

6.1. Composition of BMS and magnetite from the Jaguar deposit - implications for the deposit formation and the source of nickel

Most Ni resources are associated with magmatic sulfide or lateritic deposits (Mudd and Jowitt, 2014). On the contrary, the significant Ni resources of the Jaguar Deposit (58.9 Mt @ 0.95 % Ni) are interpreted, based on the general geology and geochemistry, to have formed through hydrothermal processes (Oliveira, 2017; Ferreira Filho et al., 2021). In addition, the Jaguar deposit also does not show typical features found in hydrothermal Ni deposits worldwide, thus raising the possibility that it could be part of an IOA-IOCG hydrothermal system. For instance, González-Álvarez et al. (2013a) presented a review of hydrothermal Ni deposits and indicated that they are frequently either hosted by mafic–ultramafic rocks, or associated with black shales (Keays et al., 2009, González-Álvarez et al. 2013b; Capistrant et al., 2015; Holwell et al., 2017). The Jaguar deposit does not fall within this classification as it is neither hosted by mafic–ultramafic rocks nor associated with black shales (Ferreira Filho et al., 2021). Although hosted within felsic rocks, the Jaguar deposit has a close spatial relationship with surrounding mafic–ultramafic layered intrusions in the Carajás Province (Fig. 1b),

which may have provided a source rock for Ni-rich fluids.

Alternatively, the Jaguar deposit may represent an originally magmatic Ni-Cu sulfide deposit that was overprinted by the regional-scale hydrothermal IOCG system of the Carajás Province. This could indeed be supported by the sulfide mineralogy, which closely resembles typical magmatic sulfide assemblage of pyrrhotite, pentlandite and chalcopyrite, at a very local scale, but variably altered by fluids into pyrite and millerite (e.g. Dare et al., 2011; Djon and Barnes, 2012; Piña et al., 2013, 2016; Duran et al., 2015). The presence of magnetite (i.e. normally<15 % modal) together with massive sulfide deposits is also a common feature (Dare et al., 2012; Boutroy et al., 2014; Duran et al., 2020). However, the abundance of magnetite and apatite (frequently more than 50 % modal in massive ores), and their ubiquitous association with Ni-mineralization at Jaguar, is highly unusual for magmatic Ni sulfide deposits (Barnes and Lightfoot, 2005). Moreover, variable sulfide mineralogy without clear signs of hydrothermal alteration, including nickel sulfides (millerite and/or pentlandite) and domains with abundant sphalerite-pyrite, pyrrhotite-pyrite, and pyrite-chalcopyrite (Ferreira Filho et al., 2021), is uncommon in magmatic sulfides. Our results for the mineral chemistry of BMS and oxides provide new constraints to help refine the genetic model for the Jaguar deposit.

6.1.1. Constraints from pyrite and chalcopyrite

Discriminant compositional diagrams have been proposed to classify BMS according to their genesis, namely magmatic versus hydrothermal origin (Duran et al., 2015, 2019; Mansur et al., 2021a). For instance, Duran et al. (2015) presented a binary plot of Co/Sb versus Se/As in pyrite which allowed discrimination between magmatic (i.e. higher ratios) and hydrothermal (i.e. lower ratios) origin. Furthermore, Duran et al. (2019) introduced a ternary diagram using Cd, Se and Ni concentrations in chalcopyrite also to assess magmatic or hydrothermal origin. In this diagram, chalcopyrite from magmatic origin displays higher Ni contents, whereas those from hydrothermal origin yield higher Cd concentrations. We have included the results obtained for pyrite and chalcopyrite from the Jaguar deposit in these discriminant diagrams, and both plot within compositional fields attributed to magmatic deposits (Fig. 11a and 11b). Although this may suggest a straightforward answer indicating a magmatic origin, recent results for hydrothermal pyrite and chalcopyrite from IOCG deposits from the Candelaria-Punta del Cobre district (del Real et al., 2020) also plot within magmatic fields in these diagrams. An interesting feature is that in the pyrite discriminant diagram (Fig. 11a), the Jaguar deposit and Candelaria-Punta del Cobre district results do not in fact overlap with pyrite compositions from most magmatic Ni-Cu-PGE deposits. On the contrary, results for pyrite from the Jaguar and Candelaria-Punta del Cobre district deposits define their own compositional field (IOA and IOCG), with high Co/Sb and low Se/As ratios relative to magmatic Ni-Cu-PGE deposits. This may be explained by the fact that the data used by Duran et al. (2015) for defining the compositional field for hydrothermal deposits did not include results for IOCG deposits, as they were not available at the time of their work.

Another notable feature observed in the results for pyrite from the Jaguar deposit is the typical oscillatory zonation patterns for Co, As and Se (Fig. 5). Such zonation is like those reported for pyrite from magmatic Ni-Cu-PGE deposits, where it is interpreted to form as a response to varying pyrite growth rates upon alteration of primary pyrrhotite and pentlandite (Dare et al., 2011; Djon and Barnes, 2012; Piña et al., 2013, 2016; Duran et al., 2015; Holwell et al., 2017) or exsolution of pyrite from Fe-rich sulfide (Dare et al. 2011). However, very similar oscillatory zoning patterns are also found in pyrite from the Candelaria-Punta del Cobre district deposits, and other IOA-IOCG systems (Reich et al., 2016; del Real et al., 2020; Steadman et al., 2021). Consequently, the oscillatory zonation patterns cannot be used as evidence for directly constraining a magmatic or hydrothermal origin. Nevertheless, one similarity between pyrite composition from the Jaguar and Candearia-Punta del Cobre district deposits is the very low (i.e. usually below detection limits) Rh, Ru, Ir, Os (Ir-group platinum-group elements – IPGE) contents. In contrast, pyrite formed from the alteration of magmatic sulfides typically inherits the IPGE contents from the original pyrrhotite and pentlandite upon recrystallization (Dare et al., 2011; Djon and Barnes, 2012; Piña et al., 2013, 2016; Duran et al., 2015), which is not found in the Jaguar deposit. Therefore, although most compositional characteristics of BMS do not allow for the straightforward distinction between magmatic or hydrothermal origin in the Jaguar deposit, very low IPGE contents support the latter. Our findings also highlight the risks of exclusively using discriminant diagrams for assessing the origin of BMS.

6.1.2. Constraints from magnetite

The development of discriminant diagrams using the concentration of trace elements in minerals is further explored using magnetite composition (Dupuis and Beaudoin, 2011; Dare et al., 2014, 2015; Nadoll et al., 2014; Knipping et al., 2015; Deditius et al., 2018). Therefore, our results for magnetite from the Jaguar deposit are plotted on these diagrams to help better constrain the deposit formation and assess the hypothesis of the alteration of an originally magmatic sulfide deposit. For instance, our results were plotted in the diagrams proposed by Dare et al. (2014), Dupuis and Beaudoin (2011) and Deditius et al. (2018), and these are shown in Fig. 10f and 11c, 11d, 11e and 11f.

First of all, most magnetite from the Jaguar deposit and its host rocks predominantly plots out of the compositional field for Ni-Cu massive sulfide deposits (Fig. 11c) due to its higher Si + Mg contents. This field has been shown to be robust for most massive sulfide ores from many worldwide Ni-Cu deposits (Dare et al., 2012; Boutroy et al., 2014; Ward et al., 2018; Duran et al., 2020; Smith et al., 2022) and helps to rule out that magnetite from the Jaguar sulfide-magnetite-apatite ores are magmatic sulfides in origin. The magnetite from the younger mafic dyke generation and BIF plot within expected compositional fields (Fig. 11d) in the Ca + Al + Mn vs Ti + V diagram proposed by Dupuis and Beaudoin (2011) and display typical patterns in multi-element diagrams (Fig. 10a and e) proposed by Dare et al. (2014). Therefore, their classification as typical magnetite formed from a mafic magma and associated with BIF, respectively, seems reasonable using these diagrams. However, magnetite associated with the Jaguar deposit fall within a compositional trend that varies from Fe-Ti-V deposits, for at least part of the magnetite from host rocks (granite and felsic subvolcanic) and Bt-Chl alteration, into predominantly hydrothermal for magnetite from the Mt-Ap alteration (Fig. 11d). This is indicated by progressively lower Ca, Al, Mn, Ti and V contents from the former towards the later. This compositional shift from higher to progressively lower Ca, Al, Mn, Ti and V contents has been described in several IOA and IOCG systems, especially in the Andean system (Knipping et al., 2015; Simon et al., 2018; Deditius et al., 2018; Rodriguez-Mustafa et al., 2020; Salazar et al., 2020; Palma et al., 2021). These authors have interpreted this transition to result from magnetite initially crystallized from a silicate magma, which then progressively grow from hydrothermal fluids upon rising in the crust.

The multi-element diagrams reveal that magnetite from the Jaguar deposit display strong negative Cr anomalies relative to Ni (Fig. 10). This trace-element signature is typical of magnetite formed in high-temperature hydrothermal systems (Fig. 10f), reflecting the relative immobility of Cr in hydrothermal fluids compared to that of Ni (Dare et al. 2014). However, part of magnetite from host rocks and Bt-Chl alteration display high Ti contents and Ni/Cr ratios higher than unity. Progressively lower Ni/Cr ratios and Ti contents are found in magnetite from Mt-Ap alteration (Fig. 11d). This highlights the problem of using only a few elements for discrimination, as the magnetite from the host felsic rocks that plot within igneous fields (Fig. 11d-f), due to higher Ti and V contents, shows clear textural association to the hydrothermal Bt-Chl alteration facies (Fig. 3b and 3c). However, using the full suite of trace elements on the multi-element diagram shows that magnetite from the Bt-Chl and Mt-Ap alteration assemblages (Fig. 10f) all have similar patterns, which closely resemble that of magnetite from high-

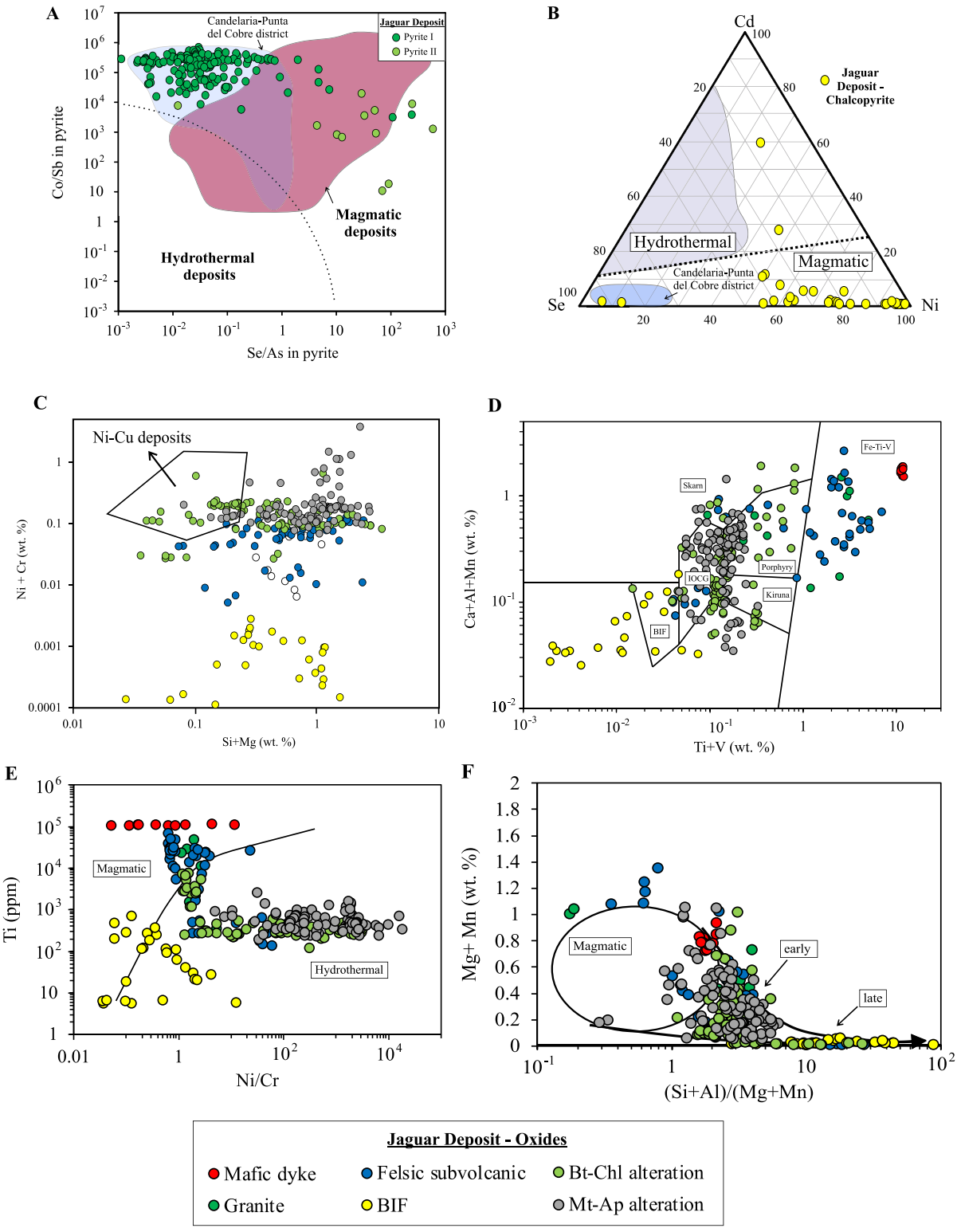

Fig. 11. Discriminant plots for sulfides and magnetite. A) Binary plot of Se/As versus Co/Sb in pyrite proposed by Duran et al. (2015). The field shown for magmatic deposits is reported by Mansur et al. (2021a). B) Ternary plot of Se, Cd and Ni in chalcopyrite proposed by Duran et al. (2019). The compositional field for chalcopyrite from the Candelaria-Punta del Cobre district is reported by del Real et al. (2020). C) Binary plot of Ni + Cr (wt. %) versus Si + Mg (wt. %) in oxides for discrimination of Ni-Cu deposits proposed by Dupuis and Beaudoin (2011). D) Binary plot of Ti + V (wt. %) versus Ca + Al + Mn (wt. %) in Fe-oxides proposed by Dupuis and Beaudoin (2011). E) Binary plot of Ni/Cr versus Ti (ppm) in magnetite proposed by Dare et al. (2014). F) Binary plot of (Si + Al)/(Mg + Mn) versus Mg + Mn (wt. %) in Fe-oxides proposed by Deditius et al. (2018).

temperature hydrothermal fluids. Moreover, recent studies argue that magnetite from IOA deposits may display higher Ti and V contents (overlapping with igneous magnetite) but has a high temperature hydrothermal origin and show high Ni/Cr ratios (Zeng et al., 2022). In these cases, Ti-rich magnetite have close textural association with hydrothermal minerals, as observed in the Jaguar deposit.

6.1.3. Origin of the Jaguar Ni deposit

The implications for the origin of the Jaguar deposit are further explored, but regardless of the genetic model, assessing the formation of the Jaguar deposit must consider the following features:

i. The deposit is associated with a regional-scale fault system, and the mineralized zones show a strong structural control. Moreover, mineralized zones are systematically accompanied by hydrothermal replacement of host rocks.
ii. The mineralized zones range from a few-centimeter veinlets to several meter-wide corridors. In both cases, sulfide minerals are systematically associated with either Bt-Chl (Type I) or Mt-Ap assemblages (Type II).
iii. Although BMS mineralogy and trace element compositions are similar to those from magmatic sulfide deposits, they are also very similar to those from IOA and IOCG deposits. Moreover, very low IPGE contents in Py from Jaguar deposit differ from those from strictly magmatic systems.
iv. The composition of magnetite ranges from higher Ca, Al, Mn, Ti and V contents in part of the host rocks and Bt-Chl alteration to much lower in Mt-Ap alteration zones, closely associated to higher-grade Ni mineralization.

Based on the observation listed above we exclude the hypothesis that the Jaguar deposit represents an altered magmatic sulfide deposit. Instead, the mineral chemistry supports a hydrothermal origin, related to the regional-scale IOCG system, as previously suggested by Oliveira (2017) and Ferreira Filho et al. (2021), based on the geology, petrography and whole rock chemistry. However, constraining the source for unusually high Ni content in hydrothermal fluids needs explanation.

6.1.4. Remobilisation of Ni by hydrothermal fluids

Considering that hydrothermal fluids have remobilized Ni to form the Jaguar deposit, as proposed by Ferreira Filho et al. (2021), the nearby Neoarchean mafic–ultramafic layered intrusions of the Carajás Province (Ferreira Filho et al., 2007) represent potential Ni sources. In this scenario, Ni would be leached from the intrusions located in the southern portion of the province (e.g., Serra da Onça, Serra do Puma Complexes; Fig. 1b), which is in agreement with the spatial distribution of Ni-rich hydrothermal systems which is restricted to the southern copper belt (e.g. Jaguar – Ferreira Filho et al., 2021; GT-34 - Siepierski, 2008; Garcia et al., 2020, Castanha – Pestilho et al., 2020; Jatobá – Veloso et al., 2020). Nickel could have been leached from Ni-bearing silicates (i.e. olivine and orthopyroxene) or from magmatic sulfides. Indeed, the transformation of primary Ni-bearing minerals, especially olivine and orthopyroxene, into secondary minerals is a recurrent feature in layered intrusions from the Carajás Province. This transformation varies from discrete zones that preserve magmatic textures to more extensively altered domains where no primary features are preserved, and have been documented in detail in previous contributions (Ferreira Filho et al., 2007; Rosa et al., 2014; Teixeira et al., 2015; Mansur and Ferreira Filho, 2016; Siepierski and Ferreira Filho, 2020; Mansur et al., 2021). However, the dissolution of magmatic sulfides and remobilization of metals would be much more likely relative to the direct leaching of Ni-bearing silicates (Keays, 1987), as also suggested by other authors (LeVaillant et al., 2015, 2016; Holwell et al., 2017). Although the behavior of the different metals varies, Lesher and Keays (2002) suggested Pt, Pd and Ni to be more readily remobilized relative to other PGE and chalcophile elements. Moreover, experimental studies support the transport of Pd in hydrothermal fluids (Sullivan et al., 2018; Sullivan et al., 2022), which could explain the concentration of Pd (<2 ppm) in pentlandite from the Jaguar deposit (Figs. 6 and 7), and the absence of the less mobile IPGE.

The remobilization of metals (e.g., Ni, Cu, Pd) and semi-metals (Se, Te, Bi, As, Sb) during the hydrothermal alteration of magmatic sulfides has also been proposed to take place in the Carajás Province. For instance, Mansur et al. (2021b) investigated the distribution of a wide-range of chalcophile elements in whole-rock and BMS from the PGE deposit hosted within the Luanga Complex (Fig. 1). The authors argued that Pd was leached from the deposit together with Se, Te and Bi during the post-cumulus alteration of the Luanga layered intrusion. Therefore, this supports the hypothesis that sulfide minerals from layered intrusions may be, at least partially, the source of some chalcophile metals for hydrothermal systems in the Carajás Province. Moreover, the relatively high contents of Te, As and Bi and their positive correlation with Ni and S in the Jaguar deposit (Ferreira Filho et al., 2021), support this hypothesis. Experimental studies (Liu et al., 2012; Tian et al., 2012; Scholten et al., 2018) indicate that Cl-ligands would enhance the Ni solubility because of higher HCl molarity. However, the fluids involved in the Jaguar deposit genesis were remarkably F-enriched, which is confirmed by previously published whole-rock analyses, and compatible with the presence of F-apatite, F-rich biotite, F-rich amphibole and fluorite within different ore types. (Oliveira, 2017; Ferreira Filho et al., 2021). However, previous contributions in hydrothermal volcanogenic massive sulfide deposits highlight that the presence of F-apatite in the system is not unequivocal proof of low-Cl concentrations in the hydrothermal system (Genna et al., 2014; Kusebauch et al., 2015 and references therein). Therefore, high F contents solely in apatite are not straightforward for constraining the F content in the Jaguar deposit, but higher F concentrations in other minerals and the presence of fluorite also favour F-bearing fluids. Thus, although further studies may provide better constraints for the composition of hydrothermal fluids in the Jaguar deposit, a F-rich system is supported by current mineralogical and mineral chemistry evidence (Oliveira, 2017; Ferreira Filho et al., 2021), and F could also act as an important ligand for Ni during remobilization by hydrothermal fluids.

The conceptual genetic model for the formation of the Jaguar deposit presented by Ferreira Filho et al. (2021) proposes that the alteration zones and the orebodies of the Jaguar deposit display an enrichment in Ni, Bi, Te, Se, Cu, Zn, S, Fe, Mg, P, F, REE and U due to the interaction of hydrothermal fluids with different rock types. In their model, Zn-enriched zones resulted from interaction with volcanic-sedimentary rocks, whereas REE-enrichments resulted from interaction with felsic subvolcanic and granitic host rocks. The authors also indicate that the abundance of REE is closely dependent on adjacent host rocks. Following this model, the nearby mafic–ultramafic layered intrusions Serra da Onça and Serra do Puma (Fig. 1b) would represent the best candidates for leaching of metals for the formation of the Jaguar deposit, especially Ni. Moreover, the layered intrusions may also be regarded as Fe sources for the hydrothermal fluids. Alternatively, the BIF from the Serra Arqueada nearby the Jaguar deposit could also represent a potential Fe source for the mineralization, but extensive alteration is not reported in the later, thus hampering this hypothesis at this stage of knowledge. This process and the different sources for metals is under investigation and will be better constrained by ongoing assessment of different isotopic signatures in the Jaguar deposit.

6.2. The Jaguar deposit as part of a Ni-rich hydrothermal system

Although our findings support the interpretation of the Jaguar as a hydrothermal deposit, its classification based on conventional genetic models is not straightforward. Among most of the genetic models proposed for different mineral deposits worldwide, it is noteworthy that the association between abundant magnetite and apatite in hydrothermal systems is typical of IOA and IOCG deposits (Hitzman et al., 1992;

Hitzman, 2000; Williams et al., 2005; Chiaradia et al., 2006; Barton, 2013; Acosta-Góngora et al., 2015; Corriveau et al., 2016; Simon et al., 2018). For instance, based on the association of magnetite and apatite in the main mineralized zones of the Jaguar deposit, Ferreira Filho et al. (2021) proposed that it may represent an IOA deposit. Nevertheless, the Jaguar is a Ni deposit, and most IOA deposits studied to date do not host large Ni resources. Indeed, several IOA deposits are commonly associated with intermediate-felsic rocks in an arc tectonic setting (Skirrow, 2022 and references therein), which is an unexpected scenario for the formation of Ni deposits (Barnes and Lightfoot, 2005). Therefore, our mineral chemistry results are compared with those from IOA deposits worldwide in order to constrain better its association with IOA and IOCG systems.

Recently, Huang et al. (2019) investigated the composition of iron oxides from several IOA and IOCG deposits. The authors reported a wide range of trace elements, which allow us to compare with our results for the Jaguar deposit. Fig. 12a shows a multi-element diagram comparing our results with those reported for magnetite from other IOA deposits (Huang and Beaudoin, 2019; Huang et al., 2019), which also plotted in the high-T hydrothermal field of Dare et al. (2014). It is remarkable that the patterns for oxides from the Jaguar deposit closely resemble those from other IOA deposits, with a slightly positive slope from least compatible to more compatible elements. A critical similarity is the strong negative Cr anomaly relative to Ni (i.e. high Ni/Cr ratios) in oxides from the Jaguar and IOA deposits worldwide. Moreover, the BMS also display similar features between IOA and IOCG systems and the Jaguar deposit as indicated by similar composition (Fig. 7) and zonation patterns (Fig. 5).

Although magnetite composition from the Jaguar deposit displays similarities with those from IOA deposits, a few differences are also observed. For instance, magnetite from the Jaguar deposit yield anomalously higher Zn, V, Mg and Co and Ni contents relative to those from

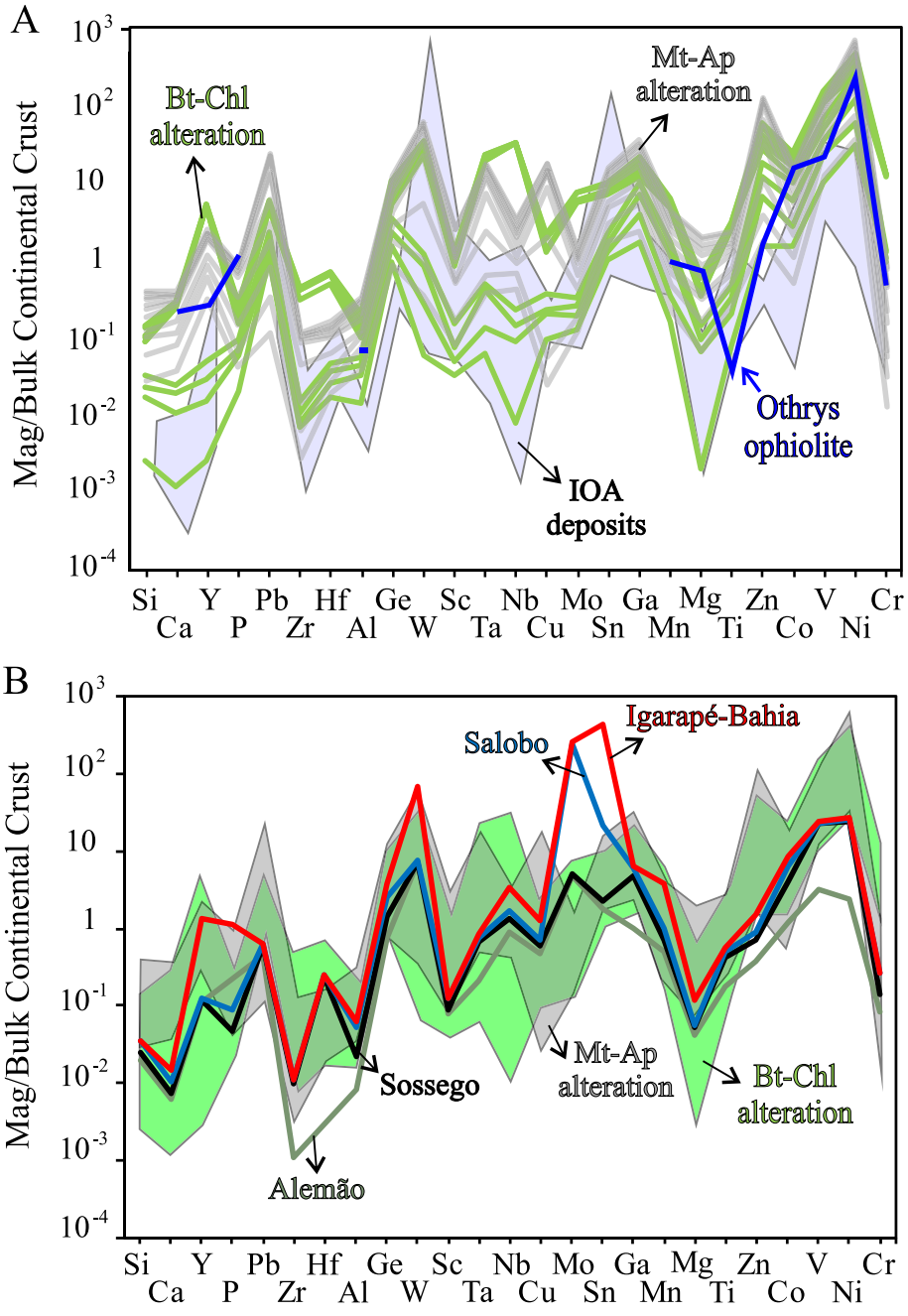

Fig. 12. Bulk continental crust-normalized multielement diagram of magnetite for comparison of the Jaguar deposit and different IOA-IOCG localities. A – Magnetite from Bt-Chl and Mt-Ap alterations from the Jaguar Deposit and compositional field for IOA deposits worldwide (Kiruna, Rektorn, El Romeral, Savage River, Pilot Knob and Pea Ridge). Average composition of magnetite from Othrys ophiolite reported by Mitsis and Economou-Eliopoulos (2001 and 2003) is shown for reference. B – Median compositional values for magnetite from IOCG deposits from the Carajás Mineral Province (Alemão, Igarapé-Bahia, Salobo and Sossego) and compositional fields for magnetite from Bt-Chl and Mt-Ap alterations from the Jaguar Deposit. Data from both IOA and IOCG deposits are reported by Huang et al. (2019). Bulk Continental Crust values from Rudnick and Gao (2003), and order of elements with increasing compatibility with magnetite to the right.

most other IOA deposits. Higher Mg, Co and Ni contents in magnetite would be, to some extent, expected within a hydrothermal Ni deposit, as these would reflect higher contents of these elements in the hydrothermal fluids. Moreover, as highlighted by Dare et al. (2014), magnetite formed from fluids that likely leached Ni from ultramafic host rocks is also richer in Mg, Co and Ni. For example, magnetite from the hydrothermal magnetite-apatite mineralization, hosted in the mantle shear zone of the Othrys ophiolite in Greece, also displays anomalously high Mg, Co and Ni contents (Mitsis and Economou-Eliopoulos 2001; Mitsis and Economou-Eliopoulos, 2003), comparable to those from the Jaguar deposit (Fig. 12a). The unusually high Mg, Co and Ni contents of magnetite from Othrys ophiolite reflects the interaction of hydrothermal fluids with ultramafic rocks (Dare et al. 2014). This agrees with our hypothesis that hydrothermal fluids that formed the Jaguar deposits have likely interacted with layered mafic–ultramafic intrusions in the Carajás Province. The unusually high Zn content of magnetite from the Jaguar deposit is compatible with sphalerite-rich zones that occur within the deposit, indicating high Zn contents in the hydrothermal system (Oliveira, 2017; Ferreira Filho et al., 2021).

In contrast, high V contents do not necessarily reflect high V concentration in the hydrothermal fluids but could rather relate to the fO_2 upon the formation of the Jaguar deposit. For instance, V^{3+}, V^{4+} and V^{5+} are stable at terrestrial oxygen fugacity (Rammensee et al., 1983; Canil, 2002), and a reduced oxidation state would be more readily incorporate V into the magnetite structure (Toplis and Corgne, 2002; Dare et al., 2014; Nadoll et al., 2014; Sievwright et al., 2017; Sievwright et al., 2020). Therefore, anomalously higher V contents in magnetite from the Jaguar deposit could indicate lower fO_2 conditions upon the formation of the deposit. Indeed, previous investigations of Ni-rich zones in IOCG deposits in the Carajás Province suggest that these also formed under relatively low fO_2 conditions (Siepierski, 2008; Garcia et al., 2020; Pestilho et al., 2020; Veloso et al., 2020; Ferreira Filho et al., 2021). For instance, Veloso et al. (2020) also proposed that high V concentrations in magnetite from the Jatobá Ni-rich IOCG deposit resulted from reduced oxygen fugacity during ore formation.

Overall, the mineral chemistry of BMS and magnetite from the Jaguar deposit resemble those of other IOA deposits worldwide. However, several features are still lacking for an unequivocal classification of the Jaguar as an IOA deposit. For instance, the Jaguar deposit does not display extensive albitization, or association to intermediate intrusions. Moreover, there is no current geochronological support for the temporal association of the Jaguar with other IOCG deposits at Carajás. Further work is required to constrain better the spatial and especially temporal relationship between the Jaguar and the IOCG deposits. Even so, we support the model that Jaguar was formed in a hydrothermal Ni-rich system, likely genetically related to IOCG deposits, in which high-temperature F-rich fluids remobilized Ni and other metal from mafic-ultramafic layered intrusions.

Some possible analogues for the Jaguar deposit are the Ni-rich zones of the IOCG systems from the Great Bear magmatic zone, located in the Northwest Territories, Canada (Ootes et al., 2010, 2017; Montreuil et al., 2013; Acosta-Góngora et al., 2014, 2015; Corriveau et al., 2016; Kelly et al., 2020). In these systems, higher Ni and Co concentrations are found associated with Ca-Fe alteration zones, interpreted as early hydrothermal stages of a large-scale system. The remobilization of a wide range o metals, which also include Ni is driven by high-salinity fluids, which could also potentially fit with the Jaguar deposit, although fluids inclusion studies are likely to help constraining this hypothesis. The distribution of trace elements in Fe-oxides from apatite-oxides-occurrences associated with the IOCG deposits from the Great Bear magmatic zone also display similarities with the Jaguar deposit (Acosta-Góngora et al., 2014). Nevertheless, the presence of albitization preceding Fe-Ca alteration (e.g. Montreuil et al., 2013; Corriveau et al., 2016), as observed in the Great Bear magmatic zone, has not yet been described in the Jaguar deposit. We support that the Jaguar deposit, which is also associated with Ca-Fe alteration, could be related to a larger scale IOCG mineral system.

6.3. The link between the Jaguar deposit and IOCG deposits in the Carajás mineral Province

Previous studies have suggested that the Jaguar deposit may be related to the IOCG hydrothermal systems in the Carajás Province (Oliveira, 2017; Ferreira Filho et al., 2021). These studies highlight the geological and geochemical similarities between the deposits thus indicating that they are part of the same regional-scale hydrothermal system. In a recent overview of the IOCG deposits in the Carajás Province, Schutesky and de Oliveira (2020) interpreted Ni-rich hydrothermal mineralization as deeper portions of the IOCG mineral system, possibly linking a deep magmatic source to progressively shallower zones. In fact, a connection between hydrothermal Ni and Cu–Au deposits in the Carajás Province was originally proposed by Siepiersky (2008) for the GT-34 deposit, but has gained recent support from contributions investigating different Ni-rich mineralization zones found in IOCG deposits in the region (Garcia et al., 2020; Pestilho et al., 2020; Veloso et al., 2020).

Following the common association in time and space of IOCG and IOA deposits, recent contributions propose that IOA deposits represent the deeper portions of IOCG systems (Knipping et al., 2015; Corriveau et al., 2016). This interpretation is also supported by deep drill core from individual deposits in Chile, where shallow IOCG mineralization grades into IOA mineralization at depth (see Simon et al., 2018 and references therein for a revision). Even though IOA deposits were not identified in the Carajás Province, previous studies have characterized magnetite-apatite-rich zones (Fe-Ca hydrothermal alteration) in IOCG deposits, which are potentially comparable to IOA systems, such as in the Sequeirinho (Monteiro et al., 2008a, 2008b) and Castanha (Pestilho et al., 2020) orebodies.

Although there is no extensive data available on trace elements in different minerals from IOCG deposits in the Carajás Province, the trace element pattern of oxides available from Salobo, Igarape-Bahia, Alemão and Sossego deposits (Huang et al., 2019) are compared with median concentrations from the Jaguar deposit (Fig. 12b). The patterns for oxides from the Jaguar deposit closely resemble those from IOCG deposits from the Carajás Province. Some scattering is observed by comparing magnetite from the Jaguar deposit and Igarape-Bahia, Alemão and Sossego IOCG deposits, however, results for Jaguar are very similar to those reported for magnetite from the Sossego deposit, including higher Ni content than other IOCG deposits. It is noteworthy that the Sossego, as for the Jaguar deposit, is part of the southern copper belt of the Carajás Province and has a close spatial association to other hydrothermal Ni (e.g. GT-34) or Ni-rich IOCG mineralization, such as the Castanha and Jatobá deposits (Fig. 1b; Garcia et al., 2020; Pestilho et al., 2020; Veloso et al., 2020). The similarity in magnetite composition is thus a favorable argument for the hypothesis that the Jaguar deposit is genetically related to other IOCG deposits within the Carajás Province.

The hypothesis of a vertical continuum from Ni mineralization in deeper portions towards IOCG deposits in shallower portions of the hydrothermal system of the Carajás Province cannot be fully constrained by our data. Nevertheless, it is noteworthy that a vertical connection is not mandatory in these systems. The work of del Real et al. (2021) proposes that IOA and IOCG deposits may represent different pulses of hydrothermal activity, not necessarily at different depths. The authors used textural and compositional variation in actinolite to demonstrate that the Candelaria IOCG deposit in Chile records an earlier IOA mineralization event overprinted by a later Cu-rich fluid forming the IOCG mineralization. Different BMS generations, such as pyrite-I and pyrite-II, observed at the Jaguar deposit support a dynamic system affected by different hydrothermal pulses, thus suggesting the model proposed for Ferreira Filho et al. (2021). For instance, pyrite-II displays a higher concentration of mobile elements (e.g. Ag, Au, Bi, Sb, Pb, Te; Fig. 7) that could have been more readily mobilized during the evolution

of the hydrothermal system. Overall, our results from the mineral chemistry strongly supports the model that the Jaguar deposit is part of the same regional scale hydrothermal system as the other IOCG deposits of the Carajás Province. However, further work is required to precisely constrain the spatial and temporal relationship of these deposits within the province.

6.4. Constraints for the formation of Fe-oxide- and apatite-rich mineral systems

The temporal and/or spatial association of IOCG deposits with apatite- and Fe-oxide-rich rocks, defining anomalously Fe-, P- and Ca-rich zones has been extensively described worldwide. There is no consensus about the genetic model for these apatite- and Fe-oxide-rich rocks, neither if these are directly related to IOCG deposit. However, three different models, ranging from magmatic to hydrothermal are currently debated in the literature. Some support an initially magmatic origin that further evolves into a magmatic-hydrothermal system via magnetite and apatite floatation from an evolving silicate magma (e.g. Knipping et al., 2015; Barra et al., 2017; Palma et al., 2019; Rodriguez-Mustafa et al., 2020, 2022), whereas others argue for a dominantly hydrothermal replacement model (Sillitoe and Burrows, 2002; Montreuil et al., 2013, 2015; Acosta-Góngora et al., 2014; Dare et al., 2015; Corriveau et al., 2016; Montreuil et al., 2016). Moreover, experimental studies also suggest that magnetite-apatite ore bodies may represent an immiscible Fe-P melt segregated during the evolution of a silicate melt (Lester et al., 2013a, 2013b; Tornos et al., 2016, 2017; Velasco et al., 2016; Hou et al., 2018; Bain et al., 2020). We briefly discuss the constraints that arise from our mineral chemistry results on these three models and present some supporting and limiting points for each of them.

6.4.1. Magmatic to hydrothermal model

In this model, magnetite first crystallizes from an intermediate to mafic melt (i.e. igneous in origin) and serve as nucleation sites for fluid bubbles upon volatile saturation (Knipping et al., 2015; Barra et al., 2017; Reich et al., 2017; Simon et al., 2018 and references therein; Palma et al., 2019; Rodriguez-Mustafa et al., 2020, 2022). The volatile phase would then further coalesce and ascent through the crust during regional extension. Upon ascension, magnetite would grow from the cooling magmatic-hydrothermal fluid. Therefore, upon pressure changes, magnetite would be precipitated in deep-seated crustal faults, forming the IOA deposits, and the fluid would further ascend transporting Fe, Cu, Au and S to shallower crustal levels to form IOCG deposits. The model is supported by trace elements in magnetite and pyrite, Fe, O and H isotopes and re-Os systematics of magnetite. A transition from higher to lower Ca, Al, Mn, Ti and V contents of magnetite is interpreted to record a transition from purely magmatic conditions to high-T magmatic-hydrothermal conditions, respectively. This variation trend was identified within the Andean IOA-IOCG deposits (Palma et al. 2018; Simon et al., 2018).

A similar compositional trend varying from higher to lower Ca, Al, Mn, Ti and V contents is also defined by magnetite from the Jaguar deposit, with the higher values in magnetite from the host rocks (i.e. associated within small pockets of hydrothermal alteration) and Bt-Chl alteration, and lower contents, for magnetite within the Mt-Ap alteration (i.e. associated with main Ni mineralization; Fig. 11d). However, high-Ti contents in magnetite alone cannot be used to unambiguously support a magmatic origin (Zeng et al., 2022). Furthermore, the overall multi-element patterns are similar for the high- and low Ti-magnetite at Jaguar and all show systematic depletion of Cr relative to Ni, distinctive of hydrothermal magnetite (Fig. 10). In addition, the high-Ti magnetite occurs mainly as disseminated grains associated with very local Bt-Chl alteration, mainly in millimetre-scale veinlets and clusters, within the host rocks of the Jaguar deposit. This is observed at different scales, but mainly in millimetre-scale veinlets and clusters. This is difficult to resolve with a model of floatation of igneous magnetite by hydrothermal magnetite. In contrast, magnetite associated with the Ni-mineralization is lower in Ti displaying a characteristically hydrothermal signature (Fig. 11d).

The mineralization at the Jaguar deposit also has much higher apatite contents (usually higher than 10 %) relative to most other IOA deposits, lacks a direct association with intermediate intrusions and extensive albitization, and contains high proportions of Ni-bearing sulfides. Therefore, although the Jaguar deposit was formed in a Ni-rich system hosted within apatite- and Fe-oxide-rich alteration zones, spatially associated with IOCG deposits, its genetic classification as an IOA deposit and the vertical connection within the IOCG system cannot be fully supported here.

6.4.2. Fe-P immiscible liquid

An alternative model for the formation of apatite- and Fe-oxide-rich rocks involves the formation of a Fe-P-rich immiscible liquid that would separate from an evolving intermediate magma (Lester et al., 2013a, 2013b; Tornos et al., 2016, 2017; Velasco et al., 2016; Hou et al., 2018; Coint et al., 2020). A variation of this model argues for the assimilation of evaporite-bearing rocks upon magma evolution and consequently segregation of a Fe-rich carbonate-sulfate immiscible melt (Bain et al., 2020). It is noteworthy that experimental conditions required to attain immiscibility for a Fe-P melt contain S and P concentrations in excess to those found in natural silicate melts (Lindsley and Epler, 2017; Simon et al., 2018). In contrast, recent contributions highlight that there are still uncertainties in terms of the conditions that would promote the formation of a Fe-P-rich liquid, especially regarding the role of Cl, F and S in the Fe-P immiscibility field at different fO_2 conditions (Brenan, 2020). However, the experiments of Hou et al. (2018) demonstrated that to form a silicate-free Fe-P-rich melt from which massive oxide-apatite ores could form, high H_2O contents in the host intermediate magma are required. In addition, Mungall et al. (2018) also report experimental results supporting the formation of an immiscible phosphatic Fe-oxide magma based on unconsolidated Fe-P-oxide material collected at Laco Sur, El Laco, thus favouring the immiscibility hypothesis.

In the case of the Jaguar deposit, the model would require not only the formation of an immiscible Fe-P liquid, but also the segregation of an immiscible sulfide liquid. For instance, experimental results by Lester et al. (2013a) support the formation of an immiscible sulfide liquid together with an immiscible Fe-P liquid, if sufficiently high S concentrations are present in the system. However, several limitations must be explained prior to suggesting this hypothesis for the formation of the magnetite-apatite-sulfide ores of the Jaguar deposit. First, the hydrothermal composition of most oxides would imply that these were later altered by exsolving hydrothermal fluids after the crystallization of the immiscible liquids (Bain et al., 2020). Moreover, the immiscible Fe-P and sulfide melts would require an simultaneous upward transport, eventually supported by fluid bubbles (Pleše et al., 2018, 2019; Yao et al., 2019; Blanks et al., 2020; Schoneveld et al., 2020). Perhaps even more importantly, the system would require significant external addition of P and S to reach an atypical composition relative to most silicate magmas. Although B-isotopes suggest the assimilation of evaporites upon the formation of IOCG deposits in the Carajás Province (Xavier et al., 2008; Riehl and Cabral, 2018; de Melo et al., 2021), which could increase P contents, the extensive external addition of S would still be required. Future contributions on different isotopic systematics in the Jaguar deposit, and especially experimental constraints on the role those different components may play in the immiscibility field for both Fe-P and sulfide melts will surely improve this debate.

6.4.3. Hydrothermal model

Another model for the formation of apatite- and Fe-oxide-rich rocks is dominantly through hydrothermal alteration. In this case, meteoric-, metamorphic or magmatic-hydrothermal fluids would scavenge metals from intermediate to mafic host rocks, or directly from magma, and

further precipitate due to changes in physic-chemical parameters (Sillitoe and Burrows, 2002; Acosta-Góngora et al., 2014, 2015; Dare et al., 2015; Montreuil et al., 2016; Corriveau et al. 2016; Tunnell et al., 2022). A similar model has been supported for the formation of the Jaguar deposit by Ferreira Filho et al. (2021), whereby they propose that the deposit formed through the remobilization of Ni by high-salinity fluids either from mafic-ultramafic layered intrusions or an originally magmatic sulfide deposit in the southern portion of the Carajás Province. High concentrations of P in the hydrothermal fluids could be explained by the assimilation of evaporite deposits, similar to that proposed for other IOCG deposits in the Carajás Province (Xavier et al., 2008; Riehl and Cabral, 2018; de Melo et al., 2021). However, the role of assimilation of evaporites in the genesis of the Jaguar deposit remains to be assessed.

6.5. Implications for the use of mineral chemistry as a provenance tool

There has been an increase in the number of studies using the mineral chemistry of oxides and sulfides to investigate different mineral systems over recent years, and it has consequently become an important tool for understanding several ore-forming processes. This is because of the advances and accessibility of micro analytical techniques, such as LA-ICP-MS, that allows the measurement of a wide range of the trace elements in various minerals (Cook et al. 2016; Sylvester and Jackson 2016). Therefore, given that the origin, composition and physico-chemical conditions of fluids/melts are driven by geological settings, and the chemical composition of minerals is a reflection of this, the compositional variation of minerals has been used to discriminate between magmatic and hydrothermal environments (Dare et al. 2014, 2015; Huang et al. 2019; Mansur et al., 2020b), distinct deposit types (Dupuis and Beaudoin 2011; Boutroy et al. 2014; Dare et al. 2012, 2014; George et al. 2015; George et al., 2018; Makvandi et al. 2016; Mao et al. 2016; Gregory et al. 2019; Mansur et al, 2020b; Barnes et al., 2020; Mansur and Barnes, 2020; Scibiorski and Cawood, 2022; Barnes et al., 2022; Caraballo et al. 2022), hydrothermal alteration (Wilkinson et al. 2015), and mineralized and barren rocks (Canil et al., 2016; Cave et al. 2017; Ward et al., 2018; Gregory et al. 2019). Recently, mineral chemistry has been applied to assess greenfield fertility during mineral exploration under covered areas using stream sediments and glacial till (Pisiak et al., 2017; Duran et al. 2019; McCurdy et al. 2022) and to vector towards known ore bodies (Baker et al. 2020; Cooke et al. 2020; Wilkinson et al. 2020; Rottier and Casanova, 2021). Although several contributions provide useful discriminant diagrams for different minerals (e.g. Fig. 11 following Dupuis and Beaudoin, 2011; Dare et al., 2014; Duran et al., 2015, 2019; Deditius et al., 2018) our results highlight the risks of using these diagrams in an uncensored manner.

Magnetite is a common accessory mineral in hydrothermal, metamorphic, and magmatic ore deposits. It has several properties that allow its use as an indicator mineral, such as a wide compositional range (Dupuis and Beaudoin, 2011; Nadoll et al., 2014; Dare et al. 2014), resistance to weathering, and occurrence in many geological settings. Moreover, magnetic properties also allow for easy recognition and recovery of the mineral. Several studies demonstrate that magnetite composition can be used as a tool for investigating petrogenetic processes (Nadoll and Koenig, 2011; Dare et al. 2012; Nadoll et al., 2014; Boutroy et al., 2014; Dare et al., 2014, 2015; Knipping et al., 2015; Deditius et al., 2018; Huang et al., 2019; Duran et al., 2020). Moreover, some contributions also highlight that magnetite composition can be used to discriminate among deposit types (Dupuis and Beaudoin, 2011; Dare et al., 2014; Nadoll et al. 2014 and references therein). However, results for magnetite from the Jaguar deposit indicate that the classification provided by discriminant diagrams is not unequivocal. For instance, results for the Jaguar deposit span across several different hydrothermal deposits following the classification by Dupuis and Beaudoin (2011) as shown in Fig. 11d, as is typical for IOA and IOCG deposits (e.g. Knipping et al. 2015).

Although indicator mineral methods have included sulfide minerals, the methods have not included systematic mineral chemistry of various sulfide minerals. These are also important indicators as they are abundant in several deposits and rare in most barren rocks, and they display distinctive trace element signatures (Large et al., 2009; Dare et al., 2010a, 2010b; Duran et al., 2015; Cook et al., 2016; George et al., 2017; Mansur et al., 2021a; Caraballo et al. 2022). However, exposure to atmospheric conditions tend to oxidize sulfide minerals (Rosso and Vaughan, 2006; Junge et al., 2019; Korges et al., 2021), thus their preservation in surface and near-surface rocks is uncommon, particularly in tropical supergene environments (Oberthür and Melcher, 2005). Nevertheless, fast burial rates in glaciated terrains and till matrix can lead to relatively impermeable conditions, which results in limited weathering. For instance, studies reported abundant sulfide minerals in till samples (Peuraniemi, 1982, 1984; Nikkarinen et al., 1984; Sarala and Peuraniemi, 2007; McClenaghan et al., 2011; McClenaghan and Paulen, 2018; Peuraniemi and Eskola, 2013; Duran et al., 2019). However, a similar problem in using discriminant diagrams for verifying a deposit type arises by considering the results for sulfides from the Jaguar deposit. Results for pyrite and chalcopyrite from the Jaguar deposit plot within fields for magmatic deposits in previously proposed discriminant diagrams (e.g. Fig. 11a and 11b following Duran et al., 2015; 2019). These diagrams were proposed under the lack of extensive data from IOCG deposits, and thus cannot be used in an uncensored manner.

We acknowledge the use of discriminant diagrams as a powerful tool for providing readily assessable information, especially applied to greenfield exploration campaigns. However, our results also highlight the risk of using only a few key elements to assess provenance, and that more complex approaches may be required when using mineral chemistry for indicator minerals as a means for assessing a deposit type. Although simple binary diagrams may provide means for separating between magmatic and hydrothermal settings (Dare et al., 2014; Duran et al., 2015, 2019; Deditius et al., 2018; Mansur et al., 2021a), these may not always be sufficiently robust for allowing for a discrimination between several deposit types. For instance, results from the Jaguar deposit could potentially lead to a misleading classification if regarded solely within binary discriminant plots. We have demonstrated that an approach using a larger number of trace elements, i.e. multi-element diagrams, is more useful to compare signatures of magnetite from different rock types and geological settings, and moreover to interpret the signature in terms of fluid composition (Fig. 11). Thus, multi-element diagrams represent a powerful tool to support petrographic descriptions, and consequently geological interpretations. In addition, multivariate statistical methods, which allow simultaneously combining a larger number of variables, are a potentially good complementary approach to binary and multi-element diagrams. The number of studies using this approach to refine discriminant diagrams for indicator minerals has increased over the past years (Sciuba et al., 2020; de Vazelhes et al., 2021; Acosta-Góngora et al., 2022; Bédard et al., 2022; Caraballo et al., 2022; Miranda et al., 2022), which is likely to help to improve our understanding on the use of indicator minerals for mineral exploration targeting.

7. Concluding remarks

We have measured the concentrations of trace elements in sulfides (pyrite, pentlandite and chalcopyrite) and magnetite from different rock types found at the Jaguar Ni deposit and surrounding areas to better constrain the petrogenetic model for the formation of this enigmatic Ni deposit. Our main findings are summarized as follows:

(1) Magnetite composition ranges from higher Ca, Al, Mn, Ti and V contents from Bt-Chl alteration pockets in the host rocks (granitic and felsic subvolcanic) and Bt-Chl alteration, into lower contents in the Mt-Ap alteration, associated with the main Ni mineralization. Combined with textural observations and multi-element

signatures of magnetite, this compositional trend is compatible with a hydrothermal origin indicating that the Bt-Chl alteration and Mt-Ap-sulfide ores are related.

(2) Pyrite and chalcopyrite have compositions that plot within compositional fields attributed to magmatic deposits in discriminant diagrams, as is also the case for BMS from other IOCG deposits worldwide. Lower IPGE contents in pyrite from the Jaguar deposit, and oscillatory zoning of Co, As and Se are also features like those found in other IOCG deposits, and support a connection between these deposits.

(3) The concentration of trace elements in magnetite associated with the Jaguar deposit is similar to those from other IOCG deposits from the Carajás Province, especially the Sossego deposit in the southern copper belt. We suggest that the Jaguar deposit could represent a Ni-rich member of the regional-scale hydrothermal IOCG system of the Carajás Province.

(4) The Neoarchean mafic–ultramafic layered intrusions of the Carajás Province represent potential Ni sources for hydrothermal remobilization. Unusually high Ni, Co, Mg contents of magnetite supports leaching of mafic–ultramafic source rocks.

(5) Results for magnetite and BMS from the Jaguar deposit indicate that the classifications provided by available binary discriminant diagrams are not unequivocal. Magnetite from the Jaguar deposit span across several different hydrothermal deposit types in discriminant diagrams, whereas BMS fall within compositional fields for magmatic deposits. We suggest that multi-element diagrams could represent a complementary approach to binary plots and provide more comprehensive classifications for the use of indicator minerals.

Declaration of Competing Interest

The authors declare that they have no known competing financial interests or personal relationships that could have appeared to influence the work reported in this paper.

Data availability

Data will be made available on request.

Acknowledgements

This work was supported by a Canada Research Chair program grant (#950-231976) to Prof. Dr. Sarah Dare (UQAC) in Geochemistry Applied to Ore Deposits. The field work and sampling were financed in part by Vale S.A. (Projeto 550398/2010-4) and analytical expenses were covered by Centaurus Metals ltd. through part of a collaborative project with Agência para o Desenvolvimento e Inovação do Setor Mineral Brasileiro – ADIMB. Cesar Ferreira Filho is a Research Fellow at CNPq (Conselho Nacional de Desenvolvimento Científico e Tecnológico - Processo 302465/2019-7) and acknowledges the continuous support by the Coordenação de Aperfeiçoamento de Pessoal de Nível Superior - Brasil (CAPES) - Finance Code 001. This manuscript benefited from insightful comments from two anonymous reviewers, and careful editorial handling by the editors Dr. Zhaochong Zhang and Dr. Huayong Chen.

Appendix A. Supplementary data

Supplementary data to this article can be found online at https://doi.org/10.1016/j.oregeorev.2022.105256.

References

Acosta-Góngora, P., Gleeson, S.A., Samson, I.M., Ootes, L., Corriveau, L., 2014. Trace element geochemistry of magnetite and its relationship to Cu-Bi-Co-Au-Ag-UW mineralization in the Great Bear magmatic zone, NWT, Canada. Econ. Geol. 109 (7), 1901–1928.

Acosta-Góngora, P., Gleeson, S.A., Samson, I.M., Ootes, L., Corriveau, L., 2015. Gold refining by bismuth melts in the iron oxide-dominated NICO Au-Co-Bi (±Cu±W) deposit, NWT, Canada. Econ. Geol. 110 (2), 291–314.

Acosta-Góngora, P., Potter, E.G., Lawley, C.J., Petts, D., Sparkes, G., 2022. Uraninite chemistry of the Central Mineral Belt, Labrador, Canada: Application of grain-scale unsupervised machine-learning. J. Geochem. Explor. 233, 106910.

Araújo, O.J.B., & Maia, R.G.N. (1991). Serra dos Carajás, folha SB.22-ZA, Estado do Pará. Programa Levantamentos Geologicos Básicos Do Brasil. Companhia de Pesquisa de Recursos Minerais, p. 136.

Araújo, R., Nogueira, A., 2019. Serra sul diamictite of the Carajás basin (Brazil): a Paleoproterozoic glaciation on the Amazonian craton. Geology 47, 1166–1170.

Bain, W.M., Steele-MacInnis, M., Li, K., Li, L., Mazdab, F.K., Marsh, E.E., 2020. A fundamental role of carbonate–sulfate melts in the formation of iron oxide–apatite deposits. Nat. Geosci. 13 (11), 751–757.

Baker, M.J., Wilkinson, J.J., Wilkinson, C.C., Cooke, D.R., Ireland, T., 2020. Epidote trace element chemistry as an exploration tool in the Collahuasi district, northern Chile. Econ. Geol. 115 (4), 749–770.

Barnes, S-J., & Lightfoot, P. C. (2005). Formation of magmatic nickel sulfide deposits and processes affecting their copper and platinum group element contents.

Barnes, S.-J., Mansur, E.T., Pagé, P., 2022. Differences in composition of chromites from low-Ti and high-Ti picrites of the Emeishan Large Igneous Province and comparison with chromites of the UG-2 platinum-deposit of the Bushveld complex. Lithos 106613.

Barnes, S.J., Taranovic, V., Schoneveld, L.E., Mansur, E.T., Le Vaillant, M., Dare, S., Blanks, D., 2020. The occurrence and origin of pentlandite-chalcopyrite-pyrrhotite loop textures in magmatic Ni-Cu sulfide ores. Econ. Geol. 115 (8), 1777–1798.

Barra, F., Reich, M., Selby, D., Rojas, P., Simon, A., Salazar, E., Palma, G., 2017. Unraveling the origin of the Andean IOCG clan: A Re-Os isotope approach. Ore Geol. Rev. 81, 62–78.

Barton, M.D., 2013. Iron oxide (-Cu-Au-REE-P-Ag-U-Co) systems. In: Treatise on Geochemistry, Second Edition. Elsevier Inc., pp. 515–541

Bédard, É., de Vazelhes, V.D.B., Beaudoin, G., 2022. Performance of predictive supervised classification models of trace elements in magnetite for mineral exploration. J. Geochem. Explor. 106959.

Blanks, D.E., Holwell, D.A., Fiorentini, M.L., Moroni, M., Giuliani, A., Tassara, S., Ferrari, E., 2020. Fluxing of mantle carbon as a physical agent for metallogenic fertilization of the crust. Nat. Commun. 11 (1), 1–11.

Boutroy, E., Dare, S.A., Beaudoin, G., Barnes, S.J., Lightfoot, P.C., 2014. Magnetite composition in Ni-Cu-PGE deposits worldwide: application to mineral exploration. J. Geochem. Explor. 145, 64–81.

Brenan, J.M., 2020. The magmatic forge. Nat. Geosci. 13 (11), 716–717.

Campo-Rodríguez, Y. T., Schutesky, M. E., de Oliveira, C. G., & Whitehouse, M. J. (2021). Unveiling the polyphasic evolution of the Neoarchean IOCG Salobo deposit, Carajás Mineral Province, Brazil: Insights from magnetite trace elements and sulfur isotopes. Ore Geology Reviews, 104572.

Canil, D., 2002. Vanadium in peridotites, mantle redox and tectonic environments: Archean to present. Earth Planet. Sci. Lett. 195 (1–2), 75–90.

Canil, D., Grondahl, C., Lacourse, T., Pisiak, L.K., 2016. Trace elements in magnetite from porphyry Cu–Mo–Au deposits in British Columbia, Canada. Ore Geol. Rev. 72, 1116–1128.

Capistrant, P.L., Hitzman, M.W., Wood, D., Kelly, N.M., Williams, G., Zimba, M., Kuiper, Y., Jack, D., Stein, H., 2015. Geology of the Enterprise hydrothermal nickel deposit, north-western province, Zambia. Econ. Geol. 110, 19–38.

Caraballo, E., Dare, S., Beaudoin, G., 2022. Variation of trace elements in chalcopyrite from worldwide Ni-Cu sulfide and Reef-type PGE deposits: implications for mineral exploration. Miner. Deposita 1–29.

Cave, B.J., Pitcairn, I.K., Craw, D., Large, R.R., Thompson, J.M., Johnson, S.C., 2017. A metamorphic mineral source for tungsten in the turbidite-hosted orogenic gold deposits of the Otago Schist. New Zealand. Mineralium Deposita 52 (4), 515–537.

Chiaradia, M., Banks, D., Cliff, R., Marschik, R., De Haller, A., 2006. Origin of fluids in iron oxide–copper–gold deposits: constraints from δ^{37}Cl, $^{87}Sr/^{86}Sr$i and Cl/Br. Miner. Deposita 41 (6), 565–573.

Coint, N., Keiding, J.K., Ihlen, P.M., 2020. Evidence for silicate–liquid immiscibility in monzonites and petrogenesis of associated Fe–Ti–P-rich rocks: Example from the Raftsund Intrusion, Lofoten, Northern Norway. J. Petrol. 61 (4), egaa045.

Cook, N., Ciobanu, C.L., George, L., Zhu, Z.Y., Wade, B., Ehrig, K., 2016. Trace element analysis of minerals in magmatic-hydrothermal ores by laser ablation inductively-coupled plasma mass spectrometry: Approaches and opportunities. Minerals 6 (4), 111.

Cooke, D.R., Wilkinson, J.J., Baker, M., Agnew, P., Phillips, J., Chang, Z., Martin, H., 2020. Using mineral chemistry to aid exploration: A case study from the Resolution porphyry Cu-Mo deposit, Arizona. Econom. Geol. 115 (4), 813–840.

Corriveau, L., Montreuil, J.F., Potter, E.G., 2016. Alteration facies linkages among iron oxide copper-gold, iron oxide-apatite, and affiliated deposits in the Great Bear magmatic zone, Northwest Territories, Canada. Econom. Geol. 111 (8), 2045–2072.

Craveiro, G.S., Villas, R.N., Xavier, R.P., 2019. Mineral chemistry and geothermometry of alteration zones in the IOCG Cristalino deposit, Carajás Mineral Province, Brazil. J. S. Am. Earth Sci. 92, 481–505.

Dare, S.A., Barnes, S.J., Prichard, H.M., 2010a. The distribution of platinum group elements (PGE) and other chalcophile elements among sulfides from the Creighton Ni–Cu–PGE sulfide deposit, Sudbury, Canada, and the origin of palladium in pentlandite. Miner. Deposita 45 (8), 765–793.

Dare, S.A., Barnes, S.J., Prichard, H.M., Fisher, P.C., 2010b. The timing and formation of platinum-group minerals from the Creighton Ni-Cu-platinum-group element sulfide

deposit, Sudbury, Canada: Early crystallization of PGE-rich sulfarsenides. Econ. Geol. 105 (6), 1071–1096.
Dare, S.A., Barnes, S.J., Prichard, H.M., Fisher, P.C., 2011. Chalcophile and platinum-group element (PGE) concentrations in the sulfide minerals from the McCreedy East deposit, Sudbury, Canada, and the origin of PGE in pyrite. Miner. Deposita 46 (4), 381–407.
Dare, S.A., Barnes, S.J., Beaudoin, G., 2012. Variation in trace element content of magnetite crystallized from a fractionating sulfide liquid, Sudbury, Canada: Implications for provenance discrimination. Geochim. Cosmochim. Acta 88, 27–50.
Dare, S.A., Barnes, S.J., Beaudoin, G., Méric, J., Boutroy, E., Potvin-Doucet, C., 2014. Trace elements in magnetite as petrogenetic indicators. Miner. Deposita 49 (7), 785–796.
Dare, S.A., Barnes, S.J., Beaudoin, G., 2015. Did the massive magnetite "lava flows" of El Laco (Chile) form by magmatic or hydrothermal processes? New constraints from magnetite composition by LA-ICP-MS. Miner. Deposita 50, 607–617.
de Melo, G.H., Monteiro, L.V., Xavier, R.P., Moreto, C.P., Santiago, E.S., Dufrane, S.A., Santos, A.F., 2017. Temporal evolution of the giant Salobo IOCG deposit, Carajás Province (Brazil): constraints from paragenesis of hydrothermal alteration and U-Pb geochronology. Miner. Deposita 52 (5), 709–732.
de Melo, G.H., Monteiro, L.V., Xavier, R.P., Moreto, C.P., Arquaz, R.M., Silva, M.A.D., 2019. Evolution of the Igarapé Bahia Cu-Au deposit, Carajás province (Brazil): early syngenetic chalcopyrite overprinted by IOCG mineralization. Ore Geol. Rev. 111, 102993.
de Melo, G.H.C., Monteiro, L.V.S., Hunger, R.B., Toledo, P.I.F., Xavier, R.P., Zhao, X.F., Moreto, C.P.N., 2021. Magmatic-hydrothermal fluids leaching older seafloor exhalative rocks to form the IOCG deposits of the Carajás Province, Brazil: Evidence from boron isotopes. Precambr. Res. 365, 106412.
de Vazelhes, V.D.B., Beaudoin, G., McMartin, I., Côté-Mantha, O., Boulianne-Verschelden, N., 2021. Assessment of the Amaruq gold deposit signature in glacial sediments using multivariate geochemical data analysis and indicator minerals. J. Geochem. Explor. 228, 106800.
Deditius, A.P., Reich, M., Simon, A.C., Suvorova, A., Knipping, J., Roberts, M.P., Saunders, M., 2018. Nanogeochemistry of hydrothermal magnetite. Contrib. Miner. Petrol. 173 (6), 1–20.
del Real, I., Thompson, J.F.H., Simon, A.C., Reich, M., 2020. Geochemical and isotopic signature of pyrite as a proxy for fluid source and evolution in the Candelaria-Punta del Cobre iron oxide copper-gold district, Chile. Econ. Geol. 115 (7), 1493–1518.
del Real, I., Reich, M., Simon, A.C., Deditius, A., Barra, F., Rodríguez-Mustafa, M.A., Roberts, M.P., 2021. Formation of giant iron oxide-copper-gold deposits by superimposed, episodic hydrothermal pulses. Commun. Earth Environ. 2 (1), 1–9.
Djon, M.L.N., Barnes, S.J., 2012. Changes in sulfides and platinum-group minerals with the degree of alteration in the Roby, Twilight, and High-Grade Zones of the Lac des Iles Complex, Ontario, Canada. Mineral. Depos. 47 (8), 875–896.
DOCEGEO, (1988). Revisao litoestratigráfica da Província Mineral de Carajás-Litoestratigrafia e principais depositos minerais. In: Congresso Brasileiro de Geologia, 35th, Belem, Sociedade Brasileira de Geologia, Proceedings, pp. 11–54.
Dreher, A.M., Xavier, R.P., Taylor, B.E., Martini, S.L., 2008. New geologic, fluid inclusion and stable isotope studies on the controversial Igarapé Bahia Cu–Au deposit, Carajás Province, Brazil. Miner. Depos. 43 (2), 161–184.
Dupuis, C., Beaudoin, G., 2011. Discriminant diagrams for iron oxide trace element fingerprinting of mineral deposit types. Miner. Depos. 46 (4), 319–335.
Duran, C.J., Barnes, S.J., Corkery, J.T., 2015. Chalcophile and platinum-group element distribution in pyrites from the sulfide-rich pods of the Lac des Iles Pd deposits, Western Ontario, Canada: Implications for post-cumulus re-equilibration of the ore and the use of pyrite compositions in exploration. J. Geochem. Explor. 158, 223–242.
Duran, C.J., Dubé-Loubert, H., Pagé, P., Barnes, S.J., Roy, M., Savard, D., Mansur, E.T., 2019. Applications of trace element chemistry of pyrite and chalcopyrite in glacial sediments to mineral exploration targeting: Example from the Churchill Province, northern Quebec, Canada. J. Geochem. Explor. 196, 105–130.
Duran, C.J., Barnes, S.J., Mansur, E.T., Dare, S.A., Bédard, L.P., Sluzhenikin, S.F., 2020. Magnetite chemistry by LA-ICP-MS records sulfide fractional crystallization in massive nickel-copper-platinum group element ores from the Norilsk-Talnakh mining district (Siberia, Russia): Implications for trace element partitioning into magnetite. Econ. Geol. 115 (6), 1245–1266.
Feio, G.R.L., Dall'Agnol, R., Dantas, E.L., Macambira, M.J.B., Santos, J.O.S., Althoff, F.J., & Soares, J.E.B. (2013). Archean granitoid magmatism in the Canaa dos Carajás area: implications for crustal evolution of the Carajás province, Amazonian craton, Brazil. Precambrian Research, 227, 157–185.
Ferreira Filho, C.F., de Oliveira, M.M.F., Mansur, E.T., Rosa, W.D., 2021. The Jaguar hydrothermal nickel sulfide deposit: Evidence for a nickel-rich member of IOCG-type deposits in the Carajás Mineral Province, Brazil. J. S. Am. Earth Sci. 111, 103501.
CFerreira Filho, C.F., Cançado, F., Correa, C., Macambira, E.M.B., Siepierski, L., & Brod, T.C. J. (2007). Mineralizaçoes estratiformes de EGP-Ni associadas a complexos acamadados em Carajás: os exemplos de Luanga e Serra da Onça. In: Contribuiçoes a Geologia da Amazonia, vol. 5. Publitec Gráfica & Editora, pp. 1–14.
Garcia, V.B., Schutesky, M.E., Oliveira, C.G., Whitehouse, M.J., Huhn, S.R., Augustin, C. T., 2020. The Neoarchean GT-34 Ni deposit, Carajás Mineral Province, Brazil: an atypical IOCG-related Ni sulfide mineralization. Ore Geol. Rev. 127, 103773.
Genna, D., Gaboury, D., Roy, G., 2014. Evolution of a volcanogenic hydrothermal system recorded by the behavior of LREE and Eu: Case study of the Key Tuffite at Bracemac–McLeod deposits, Matagami, Canada. Ore Geol. Rev. 63, 160–177.
George, L.L., Cook, N.J., Ciobanu, C.L., Wade, B.P., 2015. Trace and minor elements in galena: a reconnaissance LA-ICP-MS study. Am. Mineral. 100 (2–3), 548–569.
George, L.L., Cook, N.J., Ciobanu, C.L., 2017. Minor and trace elements in natural tetrahedrite-tennantite: Effects on element partitioning among base metal sulphides. Minerals 7 (2), 17.
George, L.L., Cook, N.J., Crowe, B.B., Ciobanu, C.L., 2018. Trace elements in hydrothermal chalcopyrite. Mineral. Mag. 82 (1), 59–88.
Gibbs, A.K., Wirth, K.R., Hirata, W.K., Olszewski Jr., W.J., 1986. Age and composition of the Grao Pará group volcanics, Serra dos Carajás. Rev. Bras. Geociencias 16, 201–211.
González-Álvarez, I., Sweetapple, M., Lindley, D., Kirakar, J., 2013a. Hydrothermal Ni: Doriri Creek, Papua New Guinea. Ore Geol. Rev. 52, 37–57.
González-Álvarez, I., Pirajno, F., Kerrich, R., 2013b. Hydrothermal nickel deposits: secular variation and diversity. Ore Geol. Rev. 52, 1–3.
Grainger, C.J., Groves, D.I., Tallarico, F.H.B., Fletcher, I.R., 2008. Metallogenesis of the Carajás mineral province, southern Amazon craton, Brazil: varying styles of Archean through paleoproterozoic to neoproterozoic base- and precious-metal mineralization. Ore Geol. Rev. 33, 451–489.
Gregory, D.D., Cracknell, M.J., Large, R.R., McGoldrick, P., Kuhn, S., Maslennikov, V.V., Lyons, T.W., 2019. Distinguishing ore deposit type and barren sedimentary pyrite using laser ablation-inductively coupled plasma-mass spectrometry trace element data and statistical analysis of large data sets. Econ. Geol. 114 (4), 771–786.
Hitzman, M.W., Oreskes, N., Einaudi, M.T., 1992. Geological characteristics and tectonic setting of Proterozoic iron oxide (Cu-U-Au-REE) deposits. Precambr. Res. 58, 241–287.
Hitzman, M.W. (2000). Iron oxide–Cu–Au deposits: what, where, when, and why: in: Porter.
Holwell, D., Adeyemi, Z., Ward, L.A., Smith, D.J., Graham, S.D., McDonald, I., Smith, J. W., 2017. Low temperature alteration of magmatic Ni-Cu- PGE sulfides as a source for hydrothermal Ni and PGE ores: a quantitative approach using automated mineralogy. Ore Geol. Rev. 91, 718–740.
Hou, T., Charlier, B., Holtz, F., Veksler, I., Zhang, Z., Thomas, R., Namur, O., 2018. Immiscible hydrous Fe–Ca–P melt and the origin of iron oxide-apatite ore deposits. Nat. Commun. 9 (1), 1–8.
Huang, X.W., Beaudoin, G., 2019. Textures and chemical compositions of magnetite from iron oxide copper-gold (IOCG) and kiruna-type iron oxide-apatite (IOA) deposits and their implications for ore genesis and magnetite classification schemes. Econ. Geol. 114 (5), 953–979.
Huang, X.W., Beaudoin, G., 2021. Nanoinclusions in zoned magnetite from the Sossego IOCG deposit, Carajás, Brazil: Implication for mineral zoning and magnetite origin discrimination. Ore Geol. Rev. 139, 104453.
Huang, X.W., Boutroy, É., Makvandi, S., Beaudoin, G., Corriveau, L., De Toni, A.F., 2019. Trace element composition of iron oxides from IOCG and IOA deposits: relationship to hydrothermal alteration and deposit subtypes. Miner. Deposita 54 (4), 525–552.
Huhn, S.R.B., Souza, C.D.J., Albuquerque, M.D., Leal, E.D., Brustolin, V., 1999. Descoberta do depósito Cu (Au) Cristalino: geologia e mineralização associada-Região da Serra do Rabo-Carajás-PA. SBG/Núcleo Norte. Simpósio de Geologia da Amazônia 6, 140–143.
Jochum, K.P., Nohl, U., Herwig, K., Lammel, E., Stoll, B., Hofmann, A.W., 2005. GeoReM: a new geochemical database for reference materials and isotopic standards. Geostand. Geoanal. Res. 29 (3), 333–338.
Junge, M., Oberthür, T., Kraemer, D., Melcher, F., Piña, R., Derrey, I.T., Strauss, H., 2019. Distribution of platinum-group elements in pristine and near-surface oxidized Platreef ore and the variation along strike, northern Bushveld Complex, South Africa. Mineral. Depos. 54 (6), 885–912.
Keays, R.R., 1987. Principles of mobilisation (dissolution) of metals in mafic and ultra-mafic rocks: the role of immiscible magmatic sulphides in the generation of hydrothermal gold and volcanogenic massive sulphide deposits. Ore Geol. Rev. 2, 47–63.
Keays, R.R., Jowitt, S.M., Callaghan, T., 2009. In: The avebury Ni Deposit, TasmaNia: a Case Study of an Unconventional Ni Deposit. Economic Geology Research Unit, Townsville, pp. 173–175.
Kelly, C.J., Davis, W.J., Potter, E.G., Corriveau, L., 2020. Geochemistry of hydrothermal tourmaline from IOCG occurrences in the Great Bear magmatic zone: implications for fluid source (s) and fluid composition evolution. Ore Geol. Rev. 118, 103329.
Knipping, J.L., Bilenker, L., Simon, A.C., Reich, M., Barra, F., Deditius, A., Lundstrom, C., Bindeman, I., Munizaga, R., 2015. Giant Kiruna-type deposits form by efficient flotation of magmatic magnetite suspensions. Geology 43, 591–594.
Korges, M., Junge, M., Borg, G., Oberthür, T., 2021. Supergene mobilization and redistribution of platinum-group elements in the Merensky Reef, eastern Bushveld Complex, South Africa. Canad. Mineral. 59 (6), 1381–1396.
Kusebauch, C., John, T., Whitehouse, M.J., Klemme, S., Putnis, A., 2015. Distribution of halogens between fluid and apatite during fluid-mediated replacement processes. Geochim. Cosmochim. Acta 170, 225–246.
Large, R.R., Danyushevsky, L., Hollit, C., Maslennikov, V., Meffre, S., Gilbert, S., Foster, J., 2009. Gold and trace element zonation in pyrite using a laser imaging technique: implications for the timing of gold in orogenic and Carlin-style sediment-hosted deposits. Econ. Geol. 104 (5), 635–668.
Lesher, C.M., Keays, R.R., 2002. Komatiite-associated Ni–Cu–(PGE) deposits: geology, mineralogy, geochemistry and genesis. Canadian Institute of Mining, Metallurgy and Petroleum 54, 579–618.
Lester, G.W., Clark, A.H., Kyser, T.K., Naslund, H.R., 2013a. Experiments on liquid immiscibility in silicate melts with H2O, P, S, F and Cl: implications for natural magmas. Contrib. Miner. Petrol. 166 (1), 329–349.
Lester, G.W., Kyser, T.K., Clark, A.H., Layton-Matthews, D., 2013b. Trace element partitioning between immiscible silicate melts with H2O, P, S, F, and Cl. Chem. Geol. 357, 178–185.

LeVaillant, M., Barnes, S.J., Fiorentini, M.L., Miller, J., McCaig, T.C., Muccili, P., 2015. A hydrothermal Ni-As-PGE geochemical halo around the Miitel komatiite-hosted nickel sulfide deposit, Yilgarn Craton, Western Australia. Econ. Geol. 110, 505–530.
LeVaillant, M., Saleem, A., Barnes, S.J., Fiorentini, M.L., Miller, J., Beresford, S., Perring, C., 2016. Hydrothermal remobilisation around a deformed and remobilised komatiite- hosted Ni-Cu-(PGE) deposit, Sarah's Find, Agnew Wiluna greenstone belt, Yilgarn Craton, Western Australia. Miner. Deposita 51, 288–369.
Lindsley, D.H., Epler, N., 2017. Do Fe-Ti-oxide magmas exist? Probably not! Am. Mineral. 102 (11), 2157–2169.
Liu, W., Migdisov, A., Williams-Jones, A., 2012. The stability of aqueous nickel (II) chloride complexes in hydrothermal solutions: results of UV–visible spectroscopic experiments. Geochem. Cosmochim. Acta 94, 276–290.
Macambira, E.M.B., & Ferreira Filho, C.F. (2002). Fracionamento Magmtico dos Corpos Máfico-Ultramáficos da Suíte Intrusiva Catete – sul do Pará. In: Klein, E.L., Vasquez, M.L., Rosa Costa, L.T. (Eds.), Contribuiçoes a Geologia da Amazonia, SBG-Núcleo Norte, vol. 3, pp. 105–114.
Macambira, M.J.B., Lancelot, J., 1996. Time constraints of Archean Rio Maria crust, southeastern amazonian craton, Brazil. Int. Geol. Rev. 38, 1134–1142.
Machado, N., Lindenmayer, D.H., Krough, T.E., Lindenmayer, Z.G., 1991. U-Pb geochronology of Archean magmatism and basement reactivation in the Carajás area, Amazon Shield, Brazil. Precambr. Res. 49, 1–26.
Makvandi, S., Ghasemzadeh-Barvarz, M., Beaudoin, G., Grunsky, E.C., McClenaghan, M. B., Duchesne, C., Boutroy, E., 2016. Partial least squares-discriminant analysis of trace element compositions of magnetite from various VMS deposit subtypes: Application to mineral exploration. Ore Geol. Rev. 78, 388–408.
Mansur, E.T., Barnes, S.J., 2020. The role of Te, As, Bi, Sn and Sb during the formation of platinum-group-element reef deposits: Examples from the Bushveld and Stillwater Complexes. Geochim. Cosmochim. Acta 272, 235–258.
Mansur, E.T., Barnes, S.J., Duran, C.J., Sluzhenikin, S.F., 2020b. Distribution of chalcophile and platinum-group elements among pyrrhotite, pentlandite, chalcopyrite and cubanite from the Noril'sk-Talnakh ores: Implications for the formation of platinum-group minerals. Miner. Deposita 55 (6), 1215–1232.
Mansur, E.T., Barnes, S.J., Duran, C.J., 2021a. An overview of chalcophile element contents of pyrrhotite, pentlandite, chalcopyrite, and pyrite from magmatic Ni-Cu-PGE sulfide deposits. Miner. Deposita 56 (1), 179–204.
Mansur, E., Barnes, S.J., Ferreira Filho, C.F., 2021b. The effects of post-cumulus alteration on the distribution of chalcophile elements in magmatic sulfide deposits and implications for the formation of low-S-high-PGE zones: The Luanga deposit, Carajás Mineral Province, Brazil. Canad. Mineral. 59 (6), 1453–1484.
Mansur, E.T., Ferreira Filho, C.F., 2016. Magmatic structure and geochemistry of the Luanga mafic-ultramafic complex: further constraints for the PGE-mineralized magmatism in Carajás, Brazil. Lithos 266, 28–43.
Mansur, E.T., Ferreira Filho, C.F., 2017. Chromitites from the Luanga Complex, Carajás, Brazil: stratigraphic distribution and clues to processes leading to post-magmatic alteration. Ore Geol. Rev. 90, 110–130.
Mansur, E.T., Ferreira Filho, C.F., Oliveira, D.P., 2020a. The Luanga deposit, Carajás Mineral Province, Brazil: Different styles of PGE mineralization hosted in a medium-size layered intrusion. Ore Geol. Rev. 118, 103340.
Mao, M., Rukhlov, A.S., Rowins, S.M., Spence, J., Coogan, L.A., 2016. Apatite trace element compositions: a robust new tool for mineral exploration. Econ. Geol. 111 (5), 1187–1222.
McClenaghan, M.B., Averill, S.A., Kjarsgaard, I.M., Layton-Matthews, D., & Matile, G. (2011). Indicator mineral signatures of magmatic Ni-Cu deposits, Thompson Nickel Belt, central Canada. In: McClenaghan, B., Peuraniemi, V., Lehtonen, M. (Eds.), Indicator mineral methods in mineral exploration. Workshop in the 25th International Applied Geochemistry Symposium 2011, 22–26 August 2011 Rovaniemi, Finland. Vuorimiesyhdistys, B92–4, pp. 72.
McClenaghan, M.B., Paulen, R.C., 2018. Application of till mineralogy and geochemistry to mineral exploration. Past glacial environments, Second edition, pp. 689–751.
McCurdy, M. W., Peter, J. M., McClenaghan, M. B., Gadd, M. G., Layton-Matthews, D., Leybourne, M. I., & Casselman, S. (2022). Evaluation of magnetite as an indicator mineral for porphyry Cu exploration: a case study using bedrock and stream sediments at the Casino porphyry Cu–Au–Mo deposit, Yukon, Canada. Geochemistry: Exploration, Environment, Analysis, 22(2).
Miranda, A.C.R., Beaudoin, G., Rottier, B., 2022. Scheelite chemistry from skarn systems: implications for ore-forming processes and mineral exploration. Miner. Deposita 1–29.
Mitsis, I., Economou-Eliopoulos, M., 2001. Occurrence of apatite associated with magnetite in an ophiolite complex (Othrys), Greece. Am. Mineral. 86, 1143–1150.
Mitsis, I., Economou-Eliopoulos, M., 2003. On the origin of hydroxylapatite associated with pure massive magnetite in the Othrys Ophiolite Complex, Greece. Ofioliti 28, 25–32.
Monteiro, L.V.S., Xavier, R.P., Carvalho, E.R., Hitzman, M.W., Johnson, C.A., Souza Filho, C.R., Torresi, I., 2008a. Spatial and temporal zoning of hydrothermal alteration and mineralization in the Sossego iron oxide-copper-gold deposit, Carajás mineral province, Brazil: parageneses and stable isotope constraints. Miner. Deposita 43, 129–159.
Monteiro, L.V.S., Xavier, R.P., Hitzman, M.W., Juliani, C., Souza Filho, C.R., Carvalho, E. R., 2008b. Mineral chemistry of ore and hydrothermal alteration at the Sossego iron oxide-copper-gold deposit, Carajás mineral province, Brazil. Ore Geol. Rev. 34, 317–336.
Montreuil, J.F., Potter, E.G., Corriveau, L., Davis, W.J., 2016. Element mobility patterns in magnetite-group IOCG systems: The Fab IOCG system, Northwest Territories, Canada. Ore Geol. Rev. 72, 562–584.
Moreto, C.P.N., Monteiro, L.V.S., Xavier, R.P., Creaser, R.A., DuFrane, S.A., Melo, G.H.C., Silva, M.A.D., Tassinari, C.C.G., Sato, K., 2015. Timing of multiple hydrothermal events in the iron oxide-copper-gold deposits of the Southern copper belt, Carajás province, Brazil. Miner. Deposita 50, 517–546.
Mudd, G.M., Jowitt, S.M., 2014. A detailed assessment of global nickel resource trends and endowments. Econ. Geol. 109, 1813–1841.
Mumin, A.H., Corriveau, L., Somarin, A.K., Ootes, L., 2007. Iron oxide copper-gold-type polymetallic mineralization in the Contact Lake belt, Great Bear magmatic zone, Northwest Territories, Canada. Explorat. Min. Geol. 16 (3–4), 187–208.
Mungall, J.E., Long, K., Brenan, J.M., Smythe, D., Naslund, H.R., 2018. Immiscible shoshonitic and Fe-P-oxide melts preserved in unconsolidated tephra at El Laco volcano, Chile. Geology 46 (3), 255–258.
Nadoll, P., Angerer, T., Mauk, J.L., French, D., Walshe, J., 2014. The chemistry of hydrothermal magnetite: A review. Ore Geol. Rev. 61, 1–32.
Nadoll, P., Koenig, A.E., 2011. LA-ICP-MS of magnetite: methods and reference materials. J. Anal. At. Spectrom 26 (9), 1872–1877.
Nikkarinen, M., Kallio, E., Lestinen, P., Ayräs, M., 1984. Mode of occurrence of Cu and Zn in till over three mineralized areas in Finland. J. Geochem. Explor. 21 (1–3), 239–247.
Nogueira, A.C.R. (1985). Análise faciologica e aspectos estruturais da Formaçao Aguas Claras, regiao central da Serra dos Carajás: Unpublished M.Sc. thesis. Universidade Federal do Pará (Brazil), p. 104.
Oliveira, M.M.F. (2017). Caracterizaçao e metalogenese do deposito de Ni do Jaguar, Província Mineral de Carajás. Unpublished Master Thesis, Universidade de Brasília (Brazil), 115pp.
Ootes, L., Goff, S., Jackson, V.A., Gleeson, S.A., Creaser, R.A., Samson, I.M., Mumin, A. H., 2010. Timing and thermochemical constraints on multi-element mineralisation at the Nori/RA Cu–Mo–U prospect, Great Bear magmatic zone, Northwest Territories, Canada. Mineral. Depos. 45 (6), 549–566.
Ootes, L., Snyder, D., Davis, W.J., Acosta-Góngora, P., Corriveau, L., Mumin, A.H., Jackson, V.A., 2017. A Paleoproterozoic Andean-type iron oxide copper-gold environment, the Great Bear magmatic zone, Northwest Canada. Ore Geol. Rev. 81, 123–139.
Palma, G., Barra, F., Reich, M., Valencia, V., Simon, A.C., Vervoort, J., Romero, R., 2019. Halogens, trace element concentrations, and Sr-Nd isotopes in apatite from iron oxide-apatite (IOA) deposits in the Chilean iron belt: Evidence for magmatic and hydrothermal stages of mineralization. Geochim. Cosmochim. Acta 246, 515–540.
Palma, G., Reich, M., Barra, F., Ovalle, J.T., Del Real, I., Simon, A.C., 2021. Thermal evolution of Andean iron oxide–apatite (IOA) deposits as revealed by magnetite thermometry. Sci. Rep. 11 (1), 1–9.
Paton, C., Hellstrom, J., Paul, B., Woodhead, J., Hergt, J., 2011. Iolite: Freeware for the visualisation and processing of mass spectrometric data. J. Anal. At. Spectrom 26 (12), 2508–2518.
Pestilho, A.L.S., Monteiro, L.V.S., de Melo, G.H.C., Moreto, C.P., Juliani, C., Fallick, A.E., Xavier, R.P., 2020. Stable isotopes and fluid inclusion constraints on the fluid evolution in the Bacaba and Castanha iron oxide-copper-gold deposits, Carajás Mineral Province, Brazil. Ore Geol. Rev. 126, 103738.
Peuraniemi, V., 1984. Weathering of sulphide minerals in till in some mineralized areas of Finland. In: Prospecting in Areas of Glaciated Terrain. Institution of Mining and Metallurgy, London, pp. 127–135.
Peuraniemi, V., Eskola, T., 2013. Glacial dispersal and mode of occurrence of metals in till and esker gravel at Kumpuselka, northern Finland. Geochemistry: Exploration. Environment, Analysis 13, 195–203.
Peuraniemi, V. (1982). Geochemistry of till and mode of occurrence of metals in some moraine types in Finland. In: Geological Survey of Finland, Bulletin, p 322 (75 pp.).
Pidgeon, R.T., Macambira, M.J.B., Lafon, J.M., 2000. Th-U-Pb isotopic systems and internal structures of complex zircons from an enderbite from the Pium Complex, Carajás province, Brazil: evidence for the ages of granulite facies metamorphism and the protolith of the enderbite. Chem. Geol. 166, 157–171.
Piña, R., Gervilla, F., Barnes, S.J., Ortega, L., Lunar, R., 2013. Platinum-group elements-bearing pyrite from the Aguablanca Ni-Cu sulphide deposit (SW Spain): a LA-ICP-MS study. Eur. J. Mineral. 25 (2), 241–252.
Piña, R., Gervilla, F., Barnes, S.J., Oberthür, T., Lunar, R., 2016. Platinum-group element concentrations in pyrite from the Main Sulfide Zone of the Great Dyke of Zimbabwe. Miner. Deposita 51 (7), 853–872.
Pisiak, L.K., Canil, D., Lacourse, T., Plouffe, A., Ferbey, T., 2017. Magnetite as an indicator mineral in the exploration of porphyry deposits: A case study in till near the Mount Polley Cu-Au deposit, British Columbia, Canada. Econ. Geol. 112 (4), 919–940.
Pleše, P., Higgins, M.D., Mancini, L., Lanzafame, G., Brun, F., Fife, J.L., Baker, D.R., 2018. Dynamic observations of vesiculation reveal the role of silicate crystals in bubble nucleation and growth in andesitic magmas. Lithos 296, 532–546.
Pleše, P., Higgins, M.D., Baker, D.R., Lanzafame, G., Kudrna Prašek, M., Mancini, L., Rooyakkers, S.M., 2019. Production and detachment of oxide crystal shells on bubble walls during experimental vesiculation of andesitic magmas. Contrib. Miner. Petrol. 174 (3), 1–20.
Rammensee, W., Palme, H., & Wanke, H. (1983). Experimental investigation of metal-silicate partitioning of some lithophile elements (Ta, Mn, V, Cr). In Lunar and Planetary Science Conference (Vol. 14, pp. 628-629).
Reich, M., Simon, A.C., Deditius, A., Barra, F., Chryssoulis, S., Lagas, G., Munizaga, R., 2016. Trace element signature of pyrite from the Los Colorados iron oxide-apatite (IOA) deposit, Chile: A missing link between Andean IOA and iron oxide copper-gold systems? Econ. Geol. 111 (3), 743–761.
Riehl, W., Cabral, A.R., 2018. Meta-evaporite in the Carajás mineral province, northern Brazil. Miner. Deposita 53 (7), 895–902.
Rodriguez-Mustafa, M.A., Simon, A.C., del Real, I., Thompson, J.F., Bilenker, L.D., Barra, F., Cadwell, D., 2020. A continuum from iron oxide copper-gold to iron oxide-

apatite deposits: Evidence from Fe and O stable isotopes and trace element chemistry of magnetite. Econ. Geol. 115 (7), 1443–1459.
Rodriguez-Mustafa, M.A., Simon, A.C., Bilenker, L.D., Bindeman, I., Mathur, R., Machado, E.L., 2022. The Mina Justa Iron Oxide Copper-Gold (IOCG) Deposit, Peru: Constraints on Metal and Ore Fluid Sources. Econ. Geol. 117 (3), 645–666.
Rosa, W.D. (2014). Complexos acamadados da Serra da Onça e Serra do Puma: geologia e petrologia de duas intrusoes máfico-ultramáficas com sequencia de cristalizaçao distinta na Província Arqueana de Carajás, Brasil. In: Unpublished M.Sc. Thesis. Universidade de Brasilia, Brazil, p. 65.
Rosso, K.M., Vaughan, D.J., 2006. Reactivity of sulfide mineral surfaces. Rev. Mineral. Geochem. 61 (1), 557–607.
Rottier, B., Casanova, V., 2021. Trace element composition of quartz from porphyry systems: a tracer of the mineralizing fluid evolution. Miner. Deposita 56 (5), 843–862.
Rudnick, R.L., Gao, S., Holland, H.D., Turekian, K.K., 2003. Composition of the continental crust. The crust 3, 1–64.
Salazar, E., Barra, F., Reich, M., Simon, A., Leisen, M., Palma, G., Rojo, M., 2020. Trace element geochemistry of magnetite from the Cerro Negro Norte iron oxide− apatite deposit, northern Chile. Miner. Deposita 55 (3), 409–428.
Sarala, P., Peuraniemi, V., 2007. Exploration using till geochemistry and heavy minerals in the ribbed moraine area of southern Finnish Lapland. Geochem. Explor. Environ. Anal. 7 (3), 195–205.
Scholten, L., Watenphul, A., Beermann, O., Testemale, D., Ames, D., Schmidt, C., 2018. Nickel and platinum in high-temperature H2O+HCl fluids: implications for hydrothermal mobilization. Geochem. Cosmochim. Acta 224, 187–199.
Schoneveld, L., Barnes, S.J., Godel, B., Vaillant, M.L., Yudovskaya, M.A., Kamenetsky, V., Sluzhenikin, S.F., 2020. Oxide-sulfide-melt-bubble interactions in spinel-rich taxitic rocks of the Norilsk-Talnakh intrusions, polar Siberia. Econ. Geol. 115 (6), 1305–1320.
Schutesky, M.E., de Oliveira, C.G., 2020. From the roots to the roof: an integrated model for the Neoarchean Carajás IOCG System. Brazil. Ore Geology Reviews 127, 103833.
Scibiorski, E.A., Cawood, P.A., 2022. Titanite as a petrogenetic indicator. Terra Nova.
Sciuba, M., Beaudoin, G., Grzela, D., Makvandi, S., 2020. Trace element composition of scheelite in orogenic gold deposits. Miner. Deposita 55 (6), 1149–1172.
Siepierski, L., 2008. Geologia e petrologia do prospecto GT-34: evidencia de metassomatismo de alta temperatura e baixa fO_2, Província Mineral Carajás. Universidade de Brasília (Brazil), Brasil, p. 72. Unpublished M.Sc.thesis,.
Siepierski, L., Ferreira Filho, C.F., 2020. Magmatic structure and petrology of the Vermelho Complex, Carajás Mineral Province, Brazil: Evidence for magmatic processes at the lower portion of a mafic-ultramafic intrusion. J. S. Am. Earth Sci. 102, 102700.
Sievwright, R.H., Wilkinson, J.J., O'Neill, H.S.C., Berry, A.J., 2017. Thermodynamic controls on element partitioning between titanomagnetite and andesitic–dacitic silicate melts. Contrib. Miner. Petrol. 172 (8), 1–33.
Sievwright, R.H., O'Neill, H.S.C., Tolley, J., Wilkinson, J.J., Berry, A.J., 2020. Diffusion and partition coefficients of minor and trace elements in magnetite as a function of oxygen fugacity at 1150 °C. Contrib. Miner. Petrol. 175 (5), 1–21.
Sillitoe, R.H., Burrows, D.R., 2002. New field evidence bearing on the origin of the El Laco magnetite deposit, northern Chile. Econ. Geol. 97, 1101–1109.
Silva, M.A.D., Monteiro, L.V.S., Santos, T.J.S., Moreto, C.P.N., Sousa, S.D., Faustinoni, J. M., Toledo, B.A.M., 2021. Mesoarchean migmatites of the Carajás Province: From intra-arc melting to collision. Lithos 388, 106078.
Silva, M.G., Teixeira, J.B.G., Pimentel, M.M., Vasconcelos, P.M., Arielo, A., Rocha, W.J.S. F., 2005. Geologia e mineralizaçoes de Fe–Cu–Au do Alvo GT46 (Igarape Cinzento, Carajás). In: Marini, O.J., Queiroz, E.T., Ramos, B.W. (Eds.), Caracterizaçao De Depositos Minerais Em Distritos Mineiros Da Amazonia, DNPM-CT/Mineral-ADIMB. Brasília, Brazil, pp. 94–151.
Simon, A., Knipping, J., Reich, M., Barra, F., Deditius, A., Bilenker, L., Childress, T., 2018. A holistic model that combines igneous and magmatic hydrothermal processes to explain Kiruna-type iron oxide-apatite deposits and iron oxide-copper-gold deposits as products of a single evolving ore system. Society of Economic Geologists, Special Publication 21, 89–114.
Skirrow, R.G., 2022. Iron oxide copper-gold (IOCG) deposits–A review (part 1): Settings, mineralogy, ore geochemistry and classification. Ore Geol. Rev. 140, 104569.
Smith, W.D., Maier, W.D., Andersen, J.C., Muir, D.D., Mansur, E., Bliss, I., 2022. Accessory phase perspectives for ore-forming processes and magmatic sulphide exploration in the Labrador Trough, northern Québec, Canada. Can. J. Earth Sci.
Souza, Z.S., Potrel, H., Lafon, J.M., Althoff, F.J., Pimentel, M.M., Dall'Agnol, R., Oliveira, C.G., 2001. Nd, Pb and Sr isotopes of the identidade belt, an archaean greenstone belt of the Rio Maria region (Carajás Province, Brazil): implications for the archaean geodynamic evolution of the Amazonian craton. Precambr. Res. 109, 293–315.
Souza, L.H., Vieira, E.A., 2000. Salobo 3 Alpha deposit: geology and mineralization. Hydrothermal iron oxide copper–gold and related deposits: a global perspective. Australian Mineral Foundation Adelaide, 213–224.
Steadman, J.A., Large, R.R., Olin, P.H., Danyushevsky, L.V., Meffre, S., Huston, D., Wells, T., 2021. Pyrite trace element behavior in magmatic-hydrothermal environments: An LA-ICPMS imaging study. Ore Geol. Rev. 128, 103878.
Sullivan, N.A., Zajacz, Z., Brenan, J.M., 2018. The solubility of Pd and Au in hydrous intermediate silicate melts: The effect of oxygen fugacity and the addition of Cl and S. Geochim. Cosmochim. Acta 231, 15–29.
Sullivan, N.A., Zajacz, Z., Brenan, J.M., Hinde, J.C., Tsay, A., Yin, Y., 2022. The solubility of gold and palladium in magmatic brines: Implications for PGE enrichment in mafic-ultramafic and porphyry environments. Geochim. Cosmochim. Acta 316, 230–252.
Sylvester, P.J., Jackson, S.E., 2016. A brief history of laser ablation inductively coupled plasma mass spectrometry (LA–ICP–MS). Elements 12 (5), 307–310.
Tallarico, F.H.B., Figueiredo, B.R., Groves, D.I., Kositcin, N., McNaughton, N.J., Fletcher, I.R., Rego, J.L., 2005. Geology and SHRIMP U-Pb geochronology of the Igarape Bahia deposit, Carajás copper-gold belt, Brazil: an Archean (2.57 Ga) example of iron-oxide Cu-Au-(U-REE) mineralization. Econ. Geol. 100, 7–28.
Tazava, E., DE, C.G., OLIVEIRA, Gomes, N.S., 1999. Ocorrência de ferropirosmalita nas brechas mineralizadas do depósito de Au-Cu-(±ETR-U) de Igarapé Bahia, província mineral de Carajás. Braz. J. Geol. 29 (3), 345–348.
Teixeira, A.S., Ferreira Filho, C.F., Della Giustina, M.E.S., Araújo, S.M., Silva, H.H.A.B., 2015. Geology, petrology and geochronology of the Lago Grande layered complex: evidence for a PGE-mineralized magmatic suite in the Carajas mineral province, Brazil. J. S. Am. Earth Sci. 64, 116–138.
Tian, Y., Etschmann, B., Liu, W., Borg, S., Mei, Y., Testemale, D., Johannessen, B., 2012. Speciation of nickel (II) chloride complexes in hydrothermal fluids: in situ XAS study. Chem. Geol. 334, 345–363.
Toplis, M.J., Corgne, A., 2002. An experimental study of element partitioning between magnetite, clinopyroxene and iron-bearing silicate liquids with particular emphasis on vanadium. Contrib. Miner. Petrol. 144 (1), 22–37.
Tornos, F., Velasco, F., Hanchar, J.M., 2016. Iron-rich melts, magmatic magnetite, and superheated hydrothermal systems: the El Laco deposit, Chile. Geology 44, 427–430.
Tornos, F., Velasco, F., Hanchar, J.M., 2017. The magmatic to magmatic-hydrothermal evolution of the El Laco deposit (Chile) and its implications for the genesis of magnetite-apatite deposits. Econ. Geol. 112, 1595–1628.
Torresi, I., Xavier, R.P., Bortholoto, D.F., Monteiro, L.V., 2012. Hydrothermal alteration, fluid inclusions and stable isotope systematics of the Alvo 118 iron oxide–copper–gold deposit, Carajás Mineral Province (Brazil): implications for ore genesis. Miner. Deposita 47 (3), 299–323.
Trunfull, E.F., Hagemann, S.G., Xavier, R.P., Moreto, C.P., 2020. Critical assessment of geochronological data from the Carajás Mineral Province, Brazil: implications for metallogeny and tectonic evolution. Ore Geol. Rev. 121, 103556.
Tunnell, B.N., Locmelis, M., Seeger, C., Moroni, M., Dare, S., Mathur, R., Sullivan, B., 2022. The Shepherd Mountain iron ore deposit in Southeast Missouri, USA–An extension of the Pilot Knob magmatic-hydrothermal ore system: Evidence from iron oxide chemistry. Ore Geol. Rev. 141, 104633.
Vasquez, L.V., Rosa-Costa, L.R., Silva, C.G., Ricci, P.F., Barbosa, J.O., Klein, E.L., Lopes, E.S., Macambira, E.B., Chaves, C.L., Carvalho, J.M., Oliveira, G., Anjos, G.C., & Silva, H.R. (2008a). Geologia e Recursos Minerais do Estado do Pará: Sistema de Informaçoes Geográficas-SIG: Texto explicativo dos Mapas Geologico e Tectonico e de Recursos Minerais do Estado do Pará, 1:1.000.000. In: Companhia de Pesquisa de Recursos Minerais-Serviço Geologico do Brasil. Superintendencia Regional de Belem, p. 329.
Vasquez, M.L., Sousa, C.S., & Carvalho, J.M.A. (2008b). Mapa Geologico e de Recursos Minerais do Estado do Pará, escala 1:1.000.000, Programa Geologia do Brasil (PGB), Integraçao, Atualizaçao e Difusao de Dados da Geologia do Brasil, Mapas Geologicos Estaduais. In: Companhia de Pesquisa de Recursos Minerais-Serviço Geologico do Brasil, Superintendencia Regional de Belem.
Velasco, R., Tornos, F., Hanchar, J.M., 2016. Immiscible iron- and silicarich melts and magnetite geochemistry at the El Laco volcano (northern Chile): evidence for a magmatic origin for the magnetite deposits. Econ. Geol. 79, 346–366.
Veloso, A.S.R., Monteiro, L.V.S., Juliani, C., 2020. The link between hydrothermal nickel mineralization and an iron oxide-copper–gold (IOCG) system: Constraints based on mineral chemistry in the Jatobá deposit. Carajás Province. Ore Geology Reviews 121, 103555.
Ward, L.A., Holwell, D.A., Barry, T.L., Blanks, D.E., Graham, S.D., 2018. The use of magnetite as a geochemical indicator in the exploration for magmatic Ni-Cu-PGE sulfide deposits: A case study from Munali, Zambia. J. Geochem. Explor. 188, 172–184.
Wilkinson, J.J., Chang, Z., Cooke, D.R., Baker, M.J., Wilkinson, C.C., Inglis, S., Gemmell, J.B., 2015. The chlorite proximitor: A new tool for detecting porphyry ore deposits. J. Geochem. Explor. 152, 10–26.
Wilkinson, J.J., Baker, M.J., Cooke, D.R., Wilkinson, C.C., 2020. Exploration targeting in porphyry Cu systems using propylitic mineral chemistry: A case study of the El Teniente deposit. Chile. Economic Geology 115 (4), 771–791.
Williams, P.J., Barton, M.D., Johnson, D.A., Fontboté, L., de Haller, A., Mark, G., Oliver, N.H.S., Marschik, R., 2005. Iron oxide-copper-gold deposits: Geology, space-time distribution, and possible modes of origin. Econ. Geol. 100th Anniversary Volume, 371–405.
Wirth, K.R., Gibbs, A.K., Olszewski Jr., W.J., 1986. U-Pb ages of zircons from the Grao Pará group and Serra dos Carajás granite, Pará, Brasil. Rev. Bras. Geosci. 16, 195–200.
Xavier, R.P., Monteiro, L.V.S., Souza Filho, C.R., Torresi, I., Carvalho, E.R., Dreher, A.M., Wiedenbeck, M., Trumbull, R.B., Pestilho, A.L.S., & Moreto, C.P.N. (2010). The iron oxide copper–gold deposits of the Carajás Mineral Province, Brazil: an updated and critical review. In: Porter, T.M. (Ed.), Hydrothermal Iron Oxide Copper-Gold & Related Deposits: a Global Perspective: Adelaide. Australian Miner, 285–306.
Xavier, R.P., Moreto, C.P.N., Melo, G.H.C., Toledo, P., Hunger, R., Delinardo, M., Faustinoni, J., Lopes, A., Monteiro, L.V.S., Previato, M., Jesus, S.G.P., & Huhn, S.B. (2017). Geology and metallogeny of neoarchean and paleoproterozoic copper systems of the Carajás domain, amazonian craton, Brazil. In: 14th Society of Geology Applied to Mineral Deposits (SGA) Biennial Meeting, Quebec City, Extended Abstract, vol. 3, pp. 899–902.
Xavier, R.P., Wiedenbeck, M., Trumbull, R.B., Dreher, A.M., Monteiro, L.V., Rhede, D., Torresi, I., 2008. Tourmaline B-isotopes fingerprint marine evaporites as the source of high-salinity ore fluids in iron oxide copper-gold deposits, Carajas Mineral Province (Brazil). Geology 36 (9), 743–746.
Xavier, R.P., Monteiro, L.V.S., Moreto, C.P.N., Pestilho, A.L.S., Melo, G.H.C., Silva, M.A. D., Aires, B., Ribeiro, C., Silva, F.H.F., 2012. The iron oxide copper-gold systems of

the Carajás mineral province. Brazil. Society of Economic Geologists, Special Publication, pp. 433–454.
Xie, Q.H., Zhang, Z.C., Hou, T., Cheng, Z.G., Campos, E., Wang, Z.C., Fei, X.H., 2019. New insights for the formation of Kiruna-type iron deposits by immiscible hydrous Fe-P melt and high-temperature hydrothermal processes: Evidence from El Laco deposit. Econ. Geol. 114 (1), 35–46.
Yao, Z., Mungall, J.E., Qin, K., 2019. A preliminary model for the migration of sulfide droplets in a magmatic conduit and the significance of volatiles. J. Petrol. 60 (12), 2281–2316.
Zeng, L.P., Zhao, X.F., Spandler, C., Hu, H., Hu, B., Li, J.W., Hu, Y., 2022. Origin of high-Ti magnetite in magmatic-hydrothermal systems: evidence from iron oxide-apatite (IOA) deposits of eastern china. Econ. Geol. 117 (4), 923–942.
Zucchetti, M. (2007). Rochas máficas do grupo Grao Pará e sua relaçao com a mineralizaçao de ferro dos depositos N4 E N5, Carajás, PA. In: Unpublished Ph.D. Thesis. Universidade Federal de Minas Gerais, Brazil, p. 165.